

Type-II quadrupole topological insulators

Yan-Bin Yang, Kai Li, L.-M. Duan, and Yong Xu*

Center for Quantum Information, IIIS, Tsinghua University, Beijing 100084, PR China

Modern theory of electric polarization is formulated by the Berry phase, which, when quantized, leads to topological phases of matter. Such a formulation has recently been extended to higher electric multipole moments, through the discovery of the so-called quadrupole topological insulator. It has been established by a classical electromagnetic theory that in a two-dimensional material the quantized properties for the quadrupole topological insulator should satisfy a basic relation. Here we discover a new type of quadrupole topological insulator (dubbed as type-II) that violates this relation due to the breakdown of a previously established theory that a Wannier band and an edge energy spectrum are topologically equivalent in a closed quantum system. We find that, similar to the previously discovered (referred to as type-I) quadrupole topological insulator, the type-II hosts topologically protected corner states carrying fractional corner charges. However, the edge polarizations only occur at a pair of boundaries in the type-II insulating phase, leading to the violation of the classical constraint. We propose an experimental scheme to realize such a new topological phase of matter. The existence of the new topological insulating phase means that new multipole topological insulators with distinct properties can exist in broader contexts beyond classical constraints.

Recently, the formulation of electric polarization based on the Berry phase has been extended to higher electric multipole moments, such as quadrupole moments and octupole moments [1, 2]. Similar to electric dipole moments, these multipole moments can be quantized due to crystalline symmetries, such as reflection symmetries, giving rise to multipole topological insulators. For a quadrupole topological insulator, besides the quantized quadrupole moment, the quantized edge polarization and fractional corner charge arise. Such fractional charges are associated with the appearance of the topologically protected corner states. The quadrupole topological insulator has ignited an intensive study of higher-order topological insulators with $(n - m)$ -dimensional edge states with $m > 1$ for a n -dimensional system [1–17], in stark contrast to the conventional first order topological insulators with $m = 1$. Recently, the quadrupole topological insulator has been experimentally observed [18–20].

For a two-dimensional (2D) square classical system with bulk quadrupole moments q_{xy} , a classical electromagnetic theory shows that equal amplitude edge polarizations $p_{x,y}^{\text{edge } \alpha}$ and corner charges $Q^{\text{corner } \alpha, \beta}$ can be induced so that $|q_{xy}| = |p_x^{\text{edge } \pm y}| = |p_y^{\text{edge } \pm x}| = |Q^{\text{corner } \pm x, \pm y}|$ [1, 2]. Here, $p_x^{\text{edge } \beta}$ ($p_y^{\text{edge } \alpha}$) describes the edge polarization per unit length on a square along the x (y) direction at the y -normal (x -normal) boundaries. The edges perpendicular to y (x) are labelled by the Greek letters $\beta = \pm y$ ($\alpha = \pm x$) with the sign denoting their relative positions. The currently discovered quantum quadrupole topological insulators indeed respect these relations [1, 2] [see Fig. 1(a)]. Provided that a system has bulk-independent boundary dipole moments besides the bulk quadrupole moments, the relation is summarized as $Q^{\text{corner } +x, +y} = p_y^{\text{edge } +x} + p_x^{\text{edge } +y} - q_{xy}$. While quadrupole insulating phases have been mainly studied in a system with short-range tunnelling, we con-

sider a model with long-range hopping. Similar to the model in Ref. [1], this system has reflection symmetries: $x \rightarrow -x$ and $y \rightarrow -y$, maintaining the vanishing of bulk dipole moments, while C_4 symmetry is broken. We find a novel type of quadrupole topological insulating phase where $q_{xy} = |Q^{\text{corner } \pm x, \pm y}| = |p_x^{\text{edge } \pm y}| = e/2$, but $p_y^{\text{edge } \pm x} = 0$, which is not equal to $p_x^{\text{edge } \pm y}$, violating the classical relation [see Fig. 1(b)]. The type-II insulating phase arises from the breakdown of a previously believed theory that a Wannier band can be continuously deformed into an edge energy spectrum in a quantum system, leading to edge polarizations of equal amplitude along x and y directions [1, 2, 21, 22]. It is worthwhile to note that the type-II quadrupole insulating phase is fundamentally different from the insulator with pure edge polarizations along one direction but without bulk quadrupole moments, where the classical relation is also respected.

To characterize the edge polarization (for example, the polarization along x), we consider the Wilson loop $\mathcal{W}_x = F_{x, k_x + (N_x - 1)\delta k_x} \cdots F_{x, k_x}$ and similarly for \mathcal{W}_y . Here $[F_{x, k_x}]^{mn} = \langle u_{k_x + \delta k_x}^m | u_{k_x}^n \rangle$, where $|u_{k_x}^n\rangle$ is the occupied eigenstate of a system Hamiltonian with n being the band index, $\delta k_x = 2\pi/N_x$ with N_x being the number of unit cells along x , and k_x is the quasimomentum along x due to the imposed periodic boundary condition along that direction [1, 2]. The Wannier Hamiltonian $H_{\mathcal{W}_x}$ is defined by $\mathcal{W}_x \equiv e^{iH_{\mathcal{W}_x}}$ with its eigenvalues $2\pi\nu_x$ referred to as the Wannier spectrum, where ν_x is the Wannier center that determines the polarization that each state contributes. Here, the inversion symmetry maintains the vanishing of the total polarization in the bulk [1, 2]. Let us first consider a cylinder geometry with open boundaries along y . In this case, when the Wannier spectrum exhibits isolated eigenvalues at $\nu_x = \pm 1/2$, with the corresponding eigenstates being localized at two oppo-

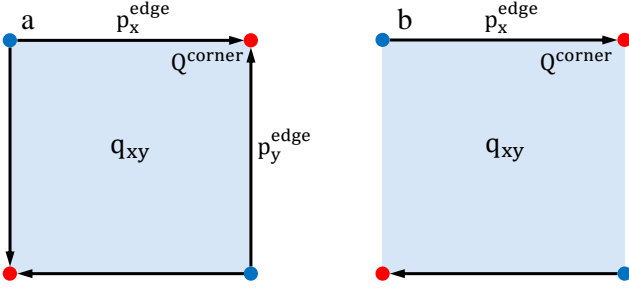


FIG. 1. (Color online) Schematics of edge polarizations and corner charges. a, Edge dipole moments exist at all boundaries in type-I quadrupole topological insulators (QTI) and b, they exist only at the boundaries perpendicular to y in type-II QTIs. Corner charges $Q^{\text{corner}} = \pm e/2$ (marked by different colors) appear in both phases.

site y -normal boundaries, the system has the boundary polarization p_x^{edge} . The appearance of the edge polarization stems from the topological property of the bulk. There are two routes to the emergence of the edge states in the Wannier spectrum. One is through the change of the topological property of the Wannier bands, the eigenvalues $\nu_x(k_y)$ of $H_{\mathcal{W}_x}(k_y)$, under periodic boundary conditions along y , by closing the Wannier band gap at $\nu_x = \pm 1/2$. An alternative route is provided by closing either the bulk energy gap or edge energy gap, resulting in an abrupt change of the quadrupole moment.

It has been believed that the Wannier band $\nu_x(k_y)$ can be continuously morphed into the edge energy spectrum localized at the x -normal boundaries [21, 22]. This means that the Wannier band and the edge energy spectrum should close their gaps simultaneously, giving rise to edge polarizations of equal amplitude at the x -normal and y -normal boundaries. However, we find that this is not necessarily true: the vanishing of the gap of the Wannier band is not necessarily associated with the vanishing of the gap of the edge energy spectrum. Hence, the edge polarization along one direction changes while that along the other direction remains, leading to the type-II quadrupole topological insulators, as detailed in Supplementary Information.

Furthermore, we find anomalous quadrupole topological phases which have the zero Berry phase of the Wannier bands (referred to as Wannier-sector polarization) but the nonzero edge polarization. This tells us that the previously introduced nested Wilson loop formalism [1, 2] cannot be used to characterize these insulating phases. Such phases arise because the Wannier Hamiltonian is fundamentally different from a static system Hamiltonian, given that the energy spectrum of the former is periodic, reminiscent of that of the effective Hamiltonian in a periodically driven system [13]. This allows the Wannier bands to close their gaps at either $\nu_x = 0$ or $\nu_x = \pm 1/2$. When the Wannier spectrum under open boundary conditions exhibit both edge states at $\nu_x = 0, \pm 1/2$, the

Berry phase vanishes; this resembles a periodically driven system, where although the traditional topological invariant of a Hamiltonian vanishes, the edge state persists [23]. In the article, we introduce a topological invariant for a Wilson line to characterize the edge polarization.

To generate the type-II quadrupole topological insulating phase, we consider a 2D crystal with four sites in each unit cell and long-range hopping between unit cells. We enforce two reflection symmetries M_x : $x \rightarrow -x$ and M_y : $y \rightarrow -y$, in order to maintain the quantization of the quadrupole moment, corner charges and edge polarizations. Specifically, the system is described by the following Hamiltonian

$$H = \sum_{\mathbf{R}} \sum_{d_x, d_y} \hat{c}_{\mathbf{R}+d_x\mathbf{e}_x+d_y\mathbf{e}_y}^\dagger h_{(d_x d_y)} \hat{c}_{\mathbf{R}}, \quad (1)$$

where $\hat{c}_{\mathbf{R}} = (\hat{c}_{\mathbf{R},1}^\dagger \hat{c}_{\mathbf{R},2}^\dagger \hat{c}_{\mathbf{R},3}^\dagger \hat{c}_{\mathbf{R},4}^\dagger)$ with $\hat{c}_{\mathbf{R},\alpha}^\dagger$ ($\hat{c}_{\mathbf{R},\alpha}$) creating (annihilating) an electron at a sublattice denoted by the index $\alpha = 1, 2, 3, 4$ within a unit cell denoted by a lattice vector $\mathbf{R} = R_x\mathbf{e}_x + R_y\mathbf{e}_y$ with R_x and R_y being integers. The sum over d_x and d_y depicts the on-site potential and the electron tunneling between distinct sublattices within a unit cell when $d_x = d_y = 0$ and the tunneling between neighboring unit cells, otherwise. For simplicity, we choose the lattice constant $a_{x,y} = 1$. Here, we consider the case with long-range hopping including up to the hopping with $(d_x = \pm 1, d_y = \pm 2)$ and $(d_x = \pm 2, d_y = \pm 1)$. To be specific, we choose $h_{(00)} = \gamma(\tau_1\sigma_0 + \tau_2\sigma_2) + \Delta\tau_3\sigma_2 + \delta\tau_3\sigma_0$, $h_{(10)} = t_1(\tau_1\sigma_0 - i\tau_2\sigma_3) + t'_1\tau_3\sigma_2$, $h_{(01)} = -it_1\tau_2\sigma_- + t'_1\tau_1\sigma_0$, $h_{(11)} = t_2(-i\tau_0\sigma_3 - i\tau_3\sigma_- + \tau_1\sigma_0 - i\tau_2\sigma_3) - it'_2\tau_2\sigma_-$, $h_{(20)} = t_2(-i\tau_3\sigma_3 + i\tau_0\sigma_1 + \tau_3\sigma_2)$, $h_{(02)} = -it_2\tau_2\sigma_- - it'_2\tau_3\sigma_-$, $h_{(21)} = t'_2(-\tau_1\sigma_0 + i\tau_2\sigma_3)$ and $h_{(12)} = it'_2\tau_2\sigma_-$, where σ, τ denote Pauli matrices for the degrees of freedom within a unit cell and $\sigma_{\pm} = \sigma_1 \pm i\sigma_2$. The other tunnelling matrices for $d_x \neq 0$ and $d_y \neq 0$ can be obtained by $h_{(-d_x-d_y)} = (h_{(d_x d_y)})^\dagger$, $\hat{m}_x h_{(d_x d_y)} \hat{m}_x^\dagger = h_{(-d_x d_y)}$ and $\hat{m}_y h_{(d_x d_y)} \hat{m}_y^\dagger = h_{(d_x -d_y)}$ required by the Hermiticity and reflection symmetries of the system with $\hat{m}_x = \tau_1\sigma_3$ and $\hat{m}_y = \tau_1\sigma_1$ for zero δ . Specifically, we set $\Delta = t_1 = 0.3$, $t'_1 = 0.2$, $t_2 = 0.15$, and $t'_2 = 0.1$. The Hamiltonian in momentum space can be found in Supplementary Information. Compared with the model in Ref. [1], our model does not preserve the time-reversal symmetry κ (κ is the complex conjugation operator) and thus the system does not have the $PT = \hat{m}_x \hat{m}_y \kappa$ symmetry, which guarantees the double degeneracy of the energy bands. Our model breaks this symmetry, lifting the energy degeneracy.

Our numerical computation shows the presence of an energy gap in momentum space energy spectra with respect to γ unless $\gamma = -0.69$ and $\gamma = 0.61$, where the energy gap vanishes. This implies that the bulk of the system exhibits the insulating property in the gapped regions at half filling. The insulating feature can also be seen in the energy spectra under open boundary condi-

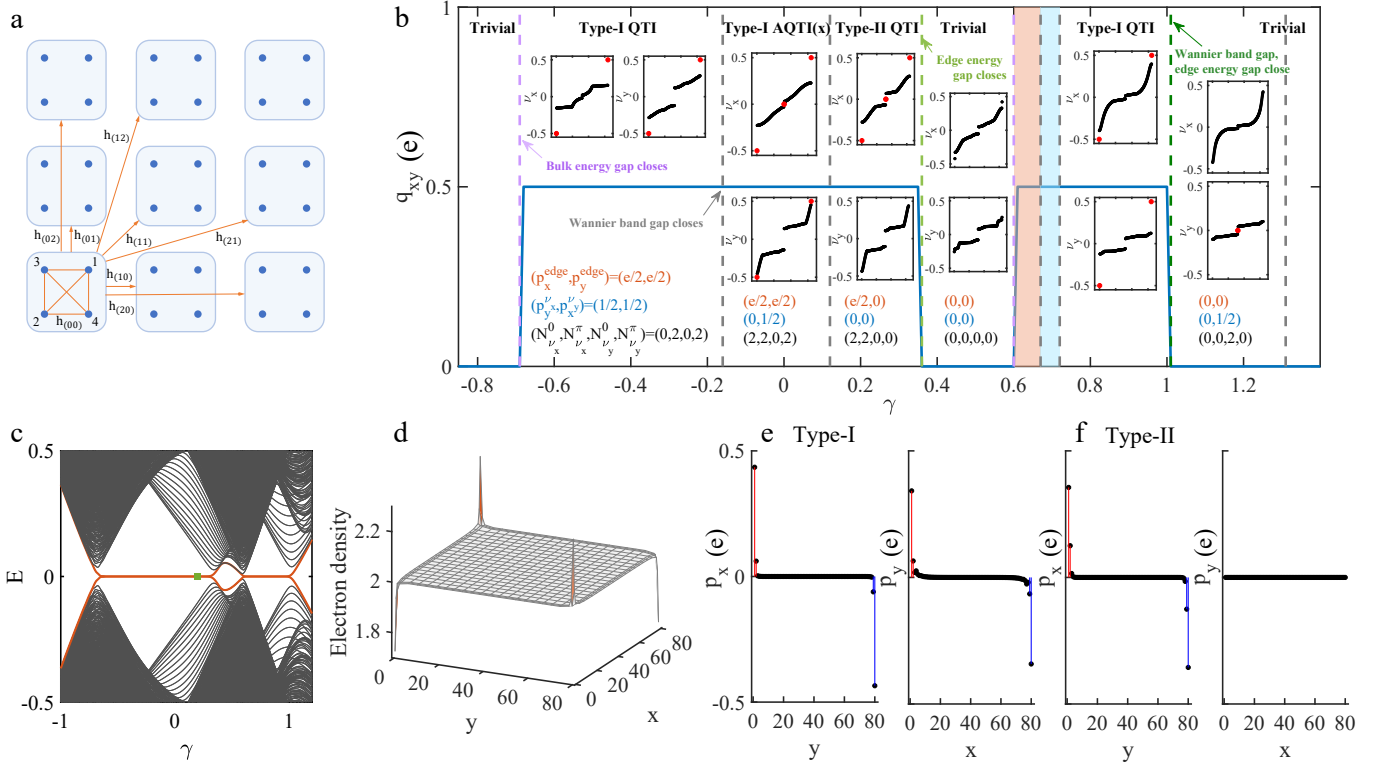


FIG. 2. (Color online) Schematics of our model, phase diagram and topological properties. a. Schematics of the tunnelling in our tight-binding model. b. Phase diagram with respect to a system parameter γ , where the quadrupole moment is plotted as a blue line. It includes topologically trivial insulator, type-I QTI, type-I anomalous quadrupole topological insulator (AQTI) (anomalousness exists in the Wannier band ν_x) and type-II QTI. The subsets display the Wannier spectrum ν_x (ν_y) in a cylinder geometry with periodic boundaries along x (y) and open ones along y (x) with the isolated Wannier centers highlighted by red circles. The edge polarization $(p_x^{\text{edge}}, p_y^{\text{edge}})$, the Wannier-sector polarization $(p_y^{\nu_x}, p_x^{\nu_y})$, the number of edge states of the Wannier Hamiltonian $N_\nu \equiv (N_{\nu_x}^0, N_{\nu_x}^\pi, N_{\nu_y}^0, N_{\nu_y}^\pi)$ are also shown. The vertical dashed lines represent the critical points where the bulk energy gap, the edge energy gap, or the Wannier spectrum gap vanish. The light red and blue regions denote the type-I AQTI(xy) (anomalousness exists in both Wannier band ν_x and ν_y) and type-I AQTI(x). Richer phase diagram for the topologically trivial phase can be found in Supplementary Information. c. The energy spectrum as a function of γ for open boundary conditions along both x and y directions with zero-energy corner modes being highlighted by a red line. d. The electron density distribution in a typical type-II QTI phase with the zero-energy corner modes marked by the green square in c. Here, a very small δ is imposed so that two corner states are occupied. e, f. The edge polarization in a type-I and a type-II QTI, respectively.

tions along both x and y directions [see Fig. 2(c)]. However, for $-0.69 < \gamma < 0.34$ and $0.61 < \gamma < 1.03$, imposing open boundaries render the appearance of four zero-energy states localized at the corners corresponding to a second-order topological insulator, where corner states exist at the boundaries of boundaries as shown in Fig. 2(d). This corner states give rise to fractional charges $\pm e/2$ localized at the corners, as detailed in the Methods section. In other parameter regions, we do not find zero-energy corner states.

To show that the insulator with zero-energy corner states is a quadrupole topological insulator, we calculate their quadrupole moments as detailed in the Methods section. Our numerical results show that the system has a quantized quadrupole moment $q_{xy} = e/2$ (protected by the reflection symmetry) in the region where the zero-energy corner modes exist, as shown in Fig. 2(b).

The change of the quadrupole moment is associated with the vanishing of either a bulk energy gap or an edge energy gap, reflecting the topological properties of the quadrupole insulating phase.

To distinguish between the type-I and type-II quadrupole topological insulators, it is necessary to characterize their edge polarization by the Wilson loop. In a torus geometry, the eigenvalues of the Wilson loop $\mathcal{W}_x(k_y)$ [similarly for $\mathcal{W}_y(k_x)$] takes the form of $e^{i2\pi\nu_x^j(k_y)}$ with $j = 1, \dots, N_{\text{occ}}$ and N_{occ} being the number of occupied bands since $\mathcal{W}_x(k_y)$ is unitary, implying that $H_{\mathcal{W}_x}(k_y)$ has eigenvalues $2\pi\nu_x^j(k_y)$. Because $e^{i2\pi\nu_x^j(k_y)}$ repeats over intervals of 1 for $\nu_x^j(k_y)$, we restrict $\nu_x^j(k_y)$ to $(-0.5, 0.5]$. Because of the reflection symmetry $M_x: x \rightarrow -x$, $\pm 2\pi\nu_x^j(k_y)$ are both eigenvalues of $H_{\mathcal{W}_x}(k_y)$, so that the Wannier centers appear in pairs $[-\nu_x^j(k_y), \nu_x^j(k_y)]$,

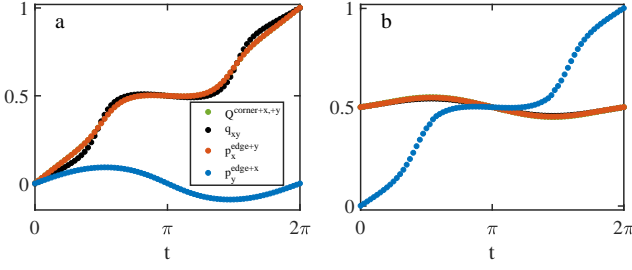


FIG. 3. (Color online) The transport of the quadrupole moment q_{xy} , corner charge $Q^{\text{corner } +x,+y}$ and edge polarization $p_{x,y}^{\text{edge}}$ over a full cycle. a, The cycle refers to the evolution of a system from a topologically trivial phase to the type-II QTI and finally return. Note that the green line is hidden behind the red one. b, The cycle refers to the evolution of a system from the type-II phase to the type-I AQTI and then return. Note that the green and black lines are hidden behind the red one. The units of all the quantities are e .

maintaining the vanishing of the bulk dipole moments in our model. The Wannier bands can be gapped with one band $\nu_x^-(k_y) \in (-0.5, 0)$ and the other $\nu_x^+(k_y) \in (0, 0.5)$ similar to a conventional band. However, it turns out that there are two gaps for the Wannier bands: one is around $\nu_x = 0$ and the other around $\nu_x = \pm 1/2$; the gaps can close at either $\nu_x = 0$ or $\nu_x = \pm 1/2$.

Fig. 2 illustrates that in the type-I phase, both Wannier spectra ν_x and ν_y under corresponding open boundary conditions (open along y and x , respectively) exhibit isolated eigenvalues at $\nu_x = \pm 1/2$, which disappear under periodic boundary conditions, implying that they are contributed by the boundary states. Their emergence indicates the presence of the dipole moments at all the four boundaries. Remarkably, in the type-II phase, only $\nu_x = \pm 1/2$ occurs but not for ν_y , implying that the dipole moments only exist at the y -normal edge but not at the x -normal one, as shown in Fig. 1(b).

Our further numerical calculation of the polarization distribution shows that the polarization, if exists, is indeed exponentially localized at the boundaries and opposite boundaries have opposite polarizations [see Fig. 2(e,f)]. While the polarization has a distribution along the direction perpendicular to a boundary, their total value for an edge is quantized, i.e., $p_{x,y}^{\text{edge}} = \pm e/2$ (see the Methods section). Despite the presence of the edge dipole moments, the total polarization vanishes as opposite boundaries have opposite edge polarizations. In the type-II phase, the polarization along y remains zero, in stark contrast to the corresponding nonzero edge polarization in the type-I phase.

Although the Wannier Hamiltonian can have the edge states at $\nu_x = \pm 1/2$ or $\nu_x = 0$, only the former contributes to the edge polarization. In fact, both of these states at $\nu_x = \pm 1/2$ or $\nu_x = 0$ can appear simultaneously. In that case, we will show that the Wannier-sector polarization is zero and thus cannot be used to characterize

these edge states. We refer to such a topological insulating phase as a type-I anomalous quadrupole topological insulator. While the type-II insulating phase is also anomalous from this perspective, we skip the "anomalous" as we do not find a type-II normal one.

The number of the edge states of the Wannier Hamiltonian $H_{\mathcal{W}_x}$ ($H_{\mathcal{W}_y}$) changes when the gap of the bulk energy spectrum $E(k_x, k_y)$, edge energy spectrum $E^{\text{edge},y}(k_x)$ [$E^{\text{edge},x}(k_y)$] at the y -normal (x -normal) edges or Wannier band $\nu_x(k_y)$ [$\nu_y(k_x)$] closes, reflecting the topological feature of the edge polarization. Associated with the vanishing of the bulk energy gap or edge energy gap is the change of the number of the edge states of the Wannier Hamiltonian corresponding to both $\nu_x = 0$ and $\nu_x = \pm 1/2$. However, when the Wannier bands close their gap at $\nu_x = 0$ or $\nu_x = \pm 1/2$, only the number of the edge states with the same eigenvalue as that where the gap vanishes changes. Specifically, the bulk energy gap closes at $\gamma = -0.69$ and $\gamma = 0.61$, leading to the phase transition between the topologically trivial phase with $N_\nu = (2, 0, 2, 0)$ and type-I quadrupole insulating phase with $N_\nu = (0, 2, 0, 2)$, and the transition between a trivial phase with $N_\nu = (0, 0, 0, 0)$ and the type-I anomalous phase with $N_\nu = (2, 2, 2, 2)$, respectively. Here, $N_\nu \equiv (N_{\nu_x}^0, N_{\nu_x}^\pi, N_{\nu_y}^0, N_{\nu_y}^\pi)$ with $N_{\nu_\lambda}^\epsilon$ ($\lambda = x, y$) denoting the number of the edge states of the Wannier Hamiltonian \mathcal{W}_λ corresponding to the eigenvalue $\epsilon = 0, \pi$. The vanishing gap of the Wannier bands divides the quadrupole insulating phase for $-0.69 < \gamma < 0.34$ into three regions: type-I QTI, type-I AQTI and type-II QTI; each gap closure gives rise to the change of the number of the corresponding edge states, as shown in Fig. 2(b). The edge energy spectrum at the y -normal boundary closes its gap at $\gamma = 0.34$, resulting in the phase transition between a trivial phase with $N_\nu = (0, 0, 0, 0)$ and the type-II QTI with $N_\nu = (2, 2, 0, 0)$.

Our results show that the Wannier bands $\nu_x(k_y)$ [$\nu_y(k_x)$] do not necessarily close their gap at $\nu = \pm 1/2$ at the same time as the edge energy spectrum localized at the x -normal (y -normal) boundaries (see Supplementary Information for details), which have been believed to be true [21, 22]. If their gaps always vanish simultaneously, there should be equal number of the edge states of the Wannier Hamiltonian \mathcal{W}_x and \mathcal{W}_y with eigenvalues $\nu = \pm 1/2$, giving rise to the same amplitude edge polarization at the x -normal and y -normal boundaries [see the case for $\gamma = 1.03$ in Fig. 2(b)]. With this violation in our model, we find the type-II phase where the dipole moments only exist at the boundaries vertical to y .

The Wannier-sector polarization were previously introduced to characterize the edge polarization of the type-I QTI. However, when it becomes anomalous, we find that a corresponding Wannier-sector polarization vanishes [see their values ($p_y^{\nu_x}, p_x^{\nu_y}$) in Fig. 2(b)], suggesting that the Wannier-sector polarization cannot uniquely identify the edge dipole moments.

To characterize the edge polarization along x (similarly along y), we will introduce a topological invariant based on the Wilson line with respect to ϵ defined as

$$\mathcal{W}_{k_x \leftarrow 0}^\epsilon(k_y) \equiv \mathcal{W}_{k_x \leftarrow 0}(k_y) e^{-i H_{W_x}^\epsilon(k_y) k_x / (2\pi)}, \quad (2)$$

where $\mathcal{W}_{k_x \leftarrow 0}(k_y) = F_{x,(k_x,k_y)} F_{x,(k_x-\delta k_x,k_y)} \cdots F_{x,(0,k_y)}$ is the Wilson line and $H_{W_x}^\epsilon(k_y) \equiv -i \log_\epsilon \mathcal{W}_{2\pi \leftarrow 0}(k_y)$ is the Wannier Hamiltonian with respect to ϵ with $\log_\epsilon(e^{i\phi}) = i\phi$ with $\epsilon \leq \phi < \epsilon + 2\pi$. The reflection symmetry leads to (the details are presented in Supplementary Information):

$$S \mathcal{W}_{\pi \leftarrow 0}^{\epsilon=0}(k_y) S^\dagger = -\mathcal{W}_{\pi \leftarrow 0}^{\epsilon=0}(k_y) \quad (3)$$

$$S \mathcal{W}_{\pi \leftarrow 0}^{\epsilon=\pi}(k_y) S^\dagger = \mathcal{W}_{\pi \leftarrow 0}^{\epsilon=\pi}(k_y), \quad (4)$$

where $S = \sigma_z$. In the basis consisting of eigenvectors of S , $\mathcal{W}_{\pi \leftarrow 0}^{\epsilon=0}(k_y) = [0, U_+^{\epsilon=0}(k_y); U_-^{\epsilon=0}(k_y), 0]$ and $\mathcal{W}_{\pi \leftarrow 0}^{\epsilon=\pi}(k_y) = [U_+^{\epsilon=\pi}(k_y), 0; 0, U_-^{\epsilon=\pi}(k_y)]$. Hence, we can define a winding number at $\epsilon = 0, \pi$ as

$$W_{\nu_x}^\epsilon = \frac{1}{2\pi i} \int_0^{2\pi} dk_y \partial_{k_y} \log U_+^\epsilon(k_y). \quad (5)$$

As presented in Supplementary Information, the winding number can change under a gauge transformation for the occupied eigenstates, since the Wilson line is defined by these eigenstates, in sharp contrast to the Floquet case, where the winding number is defined for an evolution operator [24]. It suggests that a definite physical quantity is the change of the winding number as a system parameter γ varies. During this change, the Berry phase of the occupied bands should vary continuously, as discussed in Supplementary Information. Fortunately, the quantized dipole moment is a Z_2 quantity, so that the change of the winding number is sufficient to characterize the edge polarization.

The winding number changes as the bulk energy gap and Wannier band gap close, but does not response to the closure of the edge energy gap, which is reasonable as the Wannier bands are constructed from the wave functions without any edge. However, the closure of the edge energy gap is associated with the change of the quadrupole moment. Taking into account the edge energy gap closure, we define

$$p_x^{\text{edge}}(\gamma_1) - p_x^{\text{edge}}(\gamma_0) = [(W_{\nu_x}^{\epsilon=\pi}(\gamma_1) - W_{\nu_x}^{\epsilon=\pi}(\gamma_0) - \Delta N_{q,x})/2] \bmod(1), \quad (6)$$

where $\Delta N_{q,x}$ represents the times that the quadrupole moment changes due to the gap closure of the edge energy spectrum at the boundaries perpendicular to y , when we vary γ from γ_0 to γ_1 . This shows that the topology of the bulk spectrum dictates the edge polarization as the right sides are determined by the bulk property. Provided that we start from a topologically trivial phase, i.e., $p_x^{\text{edge}}(\gamma_0) = 0$, the formula can be reduced to $p_x^{\text{edge}}(\gamma_1) = [(W_{\nu_x}^{\epsilon=\pi}(\gamma_1) - \Delta N_{q,x})/2] \bmod(1)$ by choosing

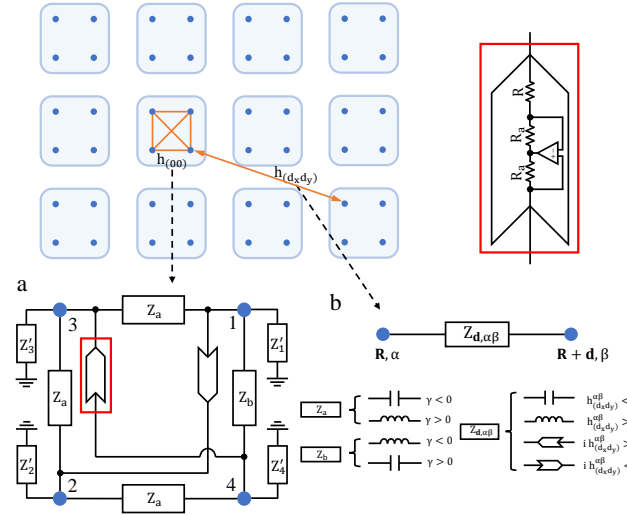


FIG. 4. (Color online) A scheme to realize our Hamiltonian in electric circuits. a, The electric device configuration to simulate the term $h_{(00)}$ within a unit cell. Here, the box labelled by Z_a or Z_b can be either a capacitor or an inductor depending on the sign of γ with their impedances being $Z_a = -1/(i\gamma)$ and $Z_b = 1/(i\gamma)$, respectively. The device in the red box denotes a negative impedance converter with current inversion (INIC), the impedance of which depends on the direction of the current. The resistance of the INIC should be taken as $R = 1/\Delta$. The boxes labelled by $Z'_{a=1,2,3,4}$ represent device configurations to eliminate the unnecessary onsite terms (see Supplementary Information). b, A suitable electric device is applied to connect two nodes: (\mathbf{R}, α) and $(\mathbf{R} + \mathbf{d}, \beta)$ for distinct unit cells. The device can be either a capacitor, or an inductor or an INIC with the impedance being $Z_{d, \alpha \beta} = i/h_{(d_x, d_y)}^{\alpha \beta}$, as shown in the lower right corner figure. Here, $\mathbf{d} = d_x \mathbf{e}_x + d_y \mathbf{e}_y$.

a gauge such that $W_{\nu_x}^{\epsilon=\pi}(\gamma_0) = 0$. As presented in Supplementary Information, this formula correctly describes the edge polarization with respect to γ .

We now discuss the pumping phenomena as a system parameter is slowly tuned. We expect the existence of anisotropic edge currents during a pumping process. To induce the change of the edge polarization, we need to break the reflection symmetry by adding a $\delta \tau_z \sigma_0$ term so that the edge polarization is not locked to be quantized. However, to maintain the vanishing of the bulk polarization, we still preserve the inversion symmetry. We also maintain the bulk and edge energy gaps during the entire cycle for adiabaticity.

Specifically, we consider the pumping process across the topologically trivial phase and type-II QTI. To achieve the pumping, we choose $\delta = 0.1 \sin(t)$ and $\gamma = 0.35 + 0.1 \cos(t)$. At $t = 0, 2\pi$, the system is in the topologically trivial phase without any edge polarization, quadrupole moments and corner charges, while at $t = \pi$, it is in the type-II QTI with $q_{xy} = |Q^{\text{corner}}| = |p_x^{\text{edge}}| = 1/2$ and $p_y^{\text{edge}} = 0$. As time progresses with changes of δ and γ , the system evolves from the topologically

trivial phase to the type-II quadrupole insulating phase and then return to the original trivial phase. At each time, we evaluate the edge polarization, corner charge and quadrupole moment (see the Methods section). We find that during an entire cycle, the edge polarization at the top boundary increases by one and at the bottom boundary it decreases by one, as shown in Fig. 3(a). This also happens for corner charges and the quadrupole moment. However, the left and right edges do not exhibit a net transport for the polarization.

We also consider the pumping process across the type-I AQTI and type-II QTI described by $\delta = 0.1 \sin(t)$ and $\gamma = 0.1 + 0.1 \cos(t)$. At $t = 0, 2\pi$, the system is in the type-II QTI phase while at $t = \pi$, the system is in the type-I AQTI phase. As time evolves over a full cycle, it turns out that only the left and right boundaries show a net change of the polarization but not for the other quantities such as the edge polarization at the top and bottom boundaries, corner charges and quadrupole moments, as shown in Fig. 3(b). Both of the pumping phenomena contrast with previous works where all boundaries, corner charges and quadrupole moments exhibit a net change during a cycle [1, 2, 25, 26]. These novel pumping phenomena indicate the peculiar features of the type-II QTI.

If we regard the adiabatic parameter t as momentum k_z in the third direction, we obtain two novel three-dimensional higher-order topological insulators characterized by a set of topological invariants consisting of the winding of the quadrupole moment and edge polarizations along two directions: $(N_{q_{xy}}, N_{p_x^{\text{edge}}}, N_{p_y^{\text{edge}}})$, where $N_O = \int_0^{2\pi} dk_z \frac{\partial O}{\partial k_z}$ with $O = q_{xy}, p_{x,y}^{\text{edge}}$. The new insulating phases correspond to $(N_{q_{xy}}, N_{p_x^{\text{edge}}}, N_{p_y^{\text{edge}}}) = (1, 1, 0)$ and $(0, 0, 1)$, respectively, which are fundamentally different from the previously found insulator with $(1, 1, 1)$. Although the phase with the winding number being $(0, 0, 1)$ has a winding for the edge polarization, it does not lead to the chiral hinge modes beyond the conventional wisdom that the presence of the winding of the polarization corresponds to a Chern insulator with chiral edge modes. In fact, in our case, it is associated with the presence of chiral edge modes in the Wannier bands, as presented in Supplementary Information.

To realize the type-II QTI, we propose a scheme to simulate the Hamiltonian in electric circuits, as illustrated in Fig. 4. We note that the type-I QTI has already been observed in electric circuits [20]. In the circuits, a Hamiltonian is simulated by a Laplacian, a matrix connecting electric potentials with currents, i.e., $\mathbf{I} = \mathbf{J}\mathbf{V}$, where \mathbf{I} and \mathbf{V} are column vectors, each entry of which denotes the corresponding current flowing into the corresponding node and the electric potential there, respectively [27]. Appropriate electric devices, such as capacitors, inductors and INICs [28, 29], are applied to connect different nodes to mimic the hopping between different sites

within or outside of a unit cell. The edge polarization and quadrupole moment can be obtained by measuring the single-point impedances of the circuit, and the existence of corner modes can be shown by measuring the resonance of two-point impedances near the corners, as detailed in Supplementary Information. Type-II QTIs may also be realized in other systems, such as solid-state materials, cold atoms and photonic crystals.

In summary, we discover a novel type of quadrupole topological insulator violating an established classical relation. This relation has been believed to be maintained in a quantum system by a previously proved theory that the Wannier band and edge energy spectrum have the same topology. However, the appearance of the type-II QTI indicates the breakdown of the theory. We also find the anomalous quadrupole insulating phases that cannot be characterized by the previously introduced Wannier-sector polarizations. We introduce a new topological invariant to characterize them. Based on the type-II insulating phase, we find new pumping phenomena, leading to novel 3D higher-order topological insulators. Our results demonstrate that new multipole topological insulators with exotic properties can exist beyond classical constraints, opening a new direction for exploring multipole topological insulators.

METHODS

The quadrupole moments. The quadrupole moment is numerically calculated based on the following formula [25, 26]

$$q_{xy} = \frac{1}{2\pi} \text{Im}[\log \langle \Psi_G | \hat{U}_2 | \Psi_G \rangle], \quad (7)$$

where $\hat{U}_2 = e^{2\pi i \sum_{\mathbf{r}} \hat{q}_{xy}(\mathbf{r})}$ with $\hat{q}_{xy}(\mathbf{r}) = xy\hat{n}(\mathbf{r})/(L_x L_y)$ being the quadrupole moment per unit cell measured with respect to $x = y = 0$ at the site \mathbf{r} , L_x and L_y are the length of the system along x and y directions, respectively, the sum is over $(x, y) \in (0, L_x] \times (0, L_y]$, $\hat{n}(\mathbf{r})$ is the number of electrons at the site \mathbf{r} and $|\Psi_G\rangle$ is the many-body ground state of a system. Our calculation is performed under periodic boundary conditions. Note that the atomic positive charge contribution has been deducted.

The corner charges. The corner charges are numerically calculated by performing the integration of the charge density over a quadrant of the system,

$$Q^{\text{corner}-x,-y} = \sum_{R_x=1}^{N_x/2} \sum_{R_y=1}^{N_y/2} \rho(\mathbf{R}), \quad (8)$$

where $\rho(\mathbf{R}) = 2e - e \sum_{n=1}^{N_{\text{occ}}} \sum_{\alpha=1}^4 |[u^n]^{\mathbf{R},\alpha}|^2$ is the charge density with the first term contributed by the atomic positive charges and the second term by the electron distribution described by the n th occupied eigenstate

$|u^n\rangle$ of our Hamiltonian under open boundary conditions with $[u^n]^{\mathbf{R},\alpha}$ being the component at the site \mathbf{R} with orbital index α .

To calculate the corner charge, we include a small δ so that the fourfold degeneracy of the zero-energy states is lifted, leading to two corner states with positive energy and the other two with negative energy. At half filling, only two corner states are occupied. Suppose the atoms contribute $+2e$ charge in each unit cell. This gives us the corner-localized fractional charges $\pm e/2$ in the limit $\delta \rightarrow 0$.

The Wannier-sector polarizations. The Wannier-sector polarization for the Wannier band ν_x^\pm (similarly for ν_y^\pm) is defined as [1, 2]

$$p_y^{\nu_x^\pm} = -\frac{1}{(2\pi)^2} \int_{BZ} d^2\mathbf{k} \mathcal{A}_{y,\mathbf{k}}^\pm, \quad (9)$$

where $\mathcal{A}_{y,\mathbf{k}} = -i\langle w_{x,\mathbf{k}}^\pm | \partial_{k_y} | w_{x,\mathbf{k}}^\pm \rangle$ is the Berry connection over the Wannier bands ν_x^\pm , respectively. $|w_{x,\mathbf{k}}^\pm\rangle = \sum_{n=1,2} |u_{\mathbf{k}}^n\rangle [\nu_{x,\mathbf{k}}^\pm]^n$ with $|u_{\mathbf{k}}^n\rangle$ being the n th occupied eigenstate of our Hamiltonian in momentum space and $[\nu_{x,\mathbf{k}}^\pm]^n$ being the n th entry of the eigenstate $|\nu_{x,\mathbf{k}}^\pm\rangle$ of the Wannier Hamiltonian in a torus geometry.

The edge polarizations. To show that the dipole moments are localized at boundaries, we calculate the polarization distribution by

$$p_x(R_y) = \sum_{j=\pm} \rho^j(R_y) \nu_x^j, \quad (10)$$

where $\rho^j(R_y) = \frac{1}{N_x} \sum_{k_x} \sum_{\alpha} \sum_{n=1}^{N_{\text{occ}}} |[u_{k_x}^n]^{R_y,\alpha} [\nu_{k_x}^j]^n|^2$ is the probability density of the hybrid Wannier functions [1, 2], $[\nu_{k_x}^j]^n$ is the n th entry of the j th eigenvector $|\nu_{k_x}^j\rangle$ of the Wannier Hamiltonian corresponding to the Wannier center ν_x^j in a cylinder geometry with open boundaries along y , and $[u_{k_x}^n]^{R_y,\alpha}$ describes the collection of entries of the n th occupied eigenstate of our Hamiltonian in the same boundary configuration. The edge polarization is defined as the sum of $p_x(R_y)$ over a half along y , i.e., $p_x^{\text{edge}-y} = \sum_{R_y=1}^{N_y/2} p_x(R_y) = -p_x^{\text{edge}+y} = -\sum_{R_y=N_y/2+1}^{N_y} p_x(R_y)$, which is quantized. Despite the presence of the edge dipole moments, there is no total polarization. The formulation of the edge polarization along y is similar.

We thank Q. Zeng and D.-L. Deng for helpful discussions. Y.B.Y., K.L. and Y.X. are supported by the start-up fund from Tsinghua University (53330300219) and the National Thousand-Young-Talents Program (042003003). We acknowledge in addition support from the Frontier Science Center for Quantum Information of the Ministry of Education of China, Tsinghua University Initiative Scientific Research Program, and the National key Research and Development Program of China (2016YFA0301902) (2016YFA0301902).

* yongxuphy@tsinghua.edu.cn

- [1] Benalcazar, W. A., Bernevig, B. A. & Hughes, T. L. Quantized electric multipole insulators. *Science* **357**, 61-66 (2017).
- [2] Benalcazar, W. A., Bernevig, B. A. & Hughes, T. L. Electric multipole moments, topological multipole moment pumping, and chiral hinge states in crystalline insulators. *Phys. Rev. B* **96**, 245115 (2017).
- [3] Song, Z., Fang, Z., & Fang, C. $(d-2)$ -Dimensional Edge States of Rotation Symmetry Protected Topological States. *Phys. Rev. Lett.* **119**, 246402 (2017).
- [4] Langbehn, J., Peng, Y., Trifunovic, L., von Oppen, F., & Brouwer, P. W. Reflection-Symmetric Second-Order Topological Insulators and Superconductors. *Phys. Rev. Lett.* **119**, 246401 (2017).
- [5] Schindler, F et al. Higher-order topological insulators. *Sci. Adv.* **4**, eaat0346 (2018).
- [6] Schindler, F et al. Higher-order topology in bismuth. *Nat. Phys.* **14**, 918-924 (2018).
- [7] Xu, Y., Xue, R. & Wan, S. Topological Corner States on Kagome Lattice Based Chiral Higher-Order Topological Insulator. Preprint at <https://arXiv.org/abs/1711.09202> (2017).
- [8] Shapourian, H., Wang, Y. & Ryu, S. Topological crystalline superconductivity and second-order topological superconductivity in nodal-loop materials. *Phys. Rev. B* **97**, 094508 (2018).
- [9] Lin, M. & Hughes, T. L. Topological quadrupolar semimetals. *Phys. Rev. B* **98**, 241103(R) (2018).
- [10] Ezawa, M. Higher-Order Topological Insulators and Semimetals on the Breathing Kagome and Pyrochlore Lattices. *Phys. Rev. Lett.* **120**, 026801 (2018).
- [11] Khalaf, E. Higher-order topological insulators and superconductors protected by inversion symmetry. *Phys. Rev. B* **97**, 205136 (2018).
- [12] Geier, M., Trifunovic, L., Hoskam, M. & Brouwer, P. W. Second-order topological insulators and superconductors with an order-two crystalline symmetry. *Phys. Rev. B* **97**, 205135 (2018).
- [13] Franca, S., van den Brink, J., & Fulga, I. C. An anomalous higher-order topological insulator. *Phys. Rev. B* **98**, 201114(R) (2018).
- [14] Yan, Z., Song, F., & Wang, Z. Majorana Corner Modes in a High-Temperature Platform. *Phys. Rev. Lett.* **121**, 096803 (2018).
- [15] Wang, Q., Liu, C. C., Lu, Y. M., & Zhang, F. High-Temperature Majorana Corner States. *Phys. Rev. Lett.* **121**, 186801 (2018).
- [16] Călugăru, D., Juričić, V., & Roy, B. Higher-order topological phases: A general principle of construction. *Phys. Rev. B* **99**, 041301(R) (2019).
- [17] Trifunovic, L., & Brouwer, P. W. Higher-Order Bulk-Boundary Correspondence for Topological Crystalline Phases. *Phys. Rev. X* **9**, 011012 (2019).
- [18] Serra-Garcia, M. et al. Observation of a phononic quadrupole topological insulator. *Nature* **555**, 342-345 (2018).
- [19] Peterson, C. W., Benalcazar, W. A., Hughes, T. L. & Bahl, G. A quantized microwave quadrupole insulator with topologically protected corner states. *Nature* **555**, 346-350 (2018).

- [20] Imhof, S. et al. Topoelectrical-circuit realization of topological corner modes. *Nat. Phys.* **14**, 925-929 (2018).
- [21] Fidkowski, L., Jackson, T. S. & Klich, I. Model characterization of gapless edge modes of topological insulators using intermediate Brillouin-zone functions. *Phys. Rev. Lett.* **107**, 036601 (2011).
- [22] Khalaf, E., Benalcazar, W. A., Hughes, T. L., & Queiroz, R. Boundary-obstructed topological phases. Preprint at <https://arXiv.org/abs/1908.00011> (2019).
- [23] Rudner, M. S., Lindner, N. H., Berg, E., & Levin, M. Anomalous edge states and the bulk-edge correspondence for periodically driven two-dimensional systems. *Phys. Rev. X* **3**, 031005 (2013).
- [24] Yao, S., Yan, Z., & Wang, Z. Topological invariants of Floquet systems: General formulation, special properties, and Floquet topological defects. *Phys. Rev. B* **96**, 195303 (2017).
- [25] Wheeler, W. A., Wagner, L. K., & Hughes, T. L. Many-Body Electric Multipole Operators in Extended Systems. Preprint at <https://arXiv.org/abs/1812.06990> (2018).
- [26] Kang, B., Shiozaki, K., & Cho, G. Y. Many-Body Order Parameters for Multipoles in Solids. Preprint at <https://arXiv.org/abs/1812.06999> (2018).
- [27] Lee, C. H. et al. Topoelectrical Circuits. *Commun. Phys.* **1**, 39 (2018).
- [28] Chen, W. K. *The Circuits and Filters Handbook*, 3rd ed. (CRC Press, Inc., Boca Raton, FL, USA, 2009).
- [29] Hofmann, T., Helbig, T., Lee, C. H., & Thomale, R. Chiral Voltage Propagation and Calibration in a Topoelectrical Chern Circuit. *Phys. Rev. Lett.* **122**, 247702 (2019).

SUPPLEMENTARY INFORMATION FOR TYPE-II QUADRUPOLE TOPOLOGICAL INSULATORS

In the Supplementary Information, we will provide the Hamiltonian in momentum space in Section 1, show the inequivalence between Wannier and edge energy spectra in Section 2, display richer physics in topologically trivial phase in Section 3, derive a topological invariant for a Wilson line in Section 4, show energy and Wannier spectra during a pumping process in Section 5, and finally detail the experimental realization in electric circuits in Section 6.

1. THE HAMILTONIAN IN MOMENTUM SPACE

We write down the explicit form of our Hamiltonian in momentum space as

$$H(\mathbf{k}) = \sum_{i,j=0}^3 g_{ij}(\mathbf{k}) \tau_i \otimes \sigma_j, \quad (\text{S1})$$

where all the nonzero g_{ij} s are given by

$$g_{01} = 2t_2 \sin(2k_x) \quad (\text{S2})$$

$$g_{03} = -4t_2 \cos(k_x) \sin(k_y) \quad (\text{S3})$$

$$g_{10} = \gamma + 2t_1 \cos(k_x) + 2t'_1 \cos(k_y) + 4t_2 \cos(k_x) \cos(k_y) - 4t'_2 \cos(2k_x) \cos(k_y) \quad (\text{S4})$$

$$g_{21} = -2t_1 \sin(k_y) - 2t_2 \sin(2k_y) - 4t'_2 \cos(k_x) \sin(k_y) + 4t'_2 \cos(k_x) \sin(2k_y) \quad (\text{S5})$$

$$g_{22} = \gamma - 2t_1 \cos(k_y) - 2t_2 \cos(2k_y) - 4t'_2 \cos(k_x) \cos(k_y) + 4t'_2 \cos(k_x) \cos(2k_y) \quad (\text{S6})$$

$$g_{23} = -2t_1 \sin(k_x) - 4t_2 \sin(k_x) \cos(k_y) + 4t'_2 \sin(2k_x) \cos(k_y) \quad (\text{S7})$$

$$g_{31} = -4t_2 \cos(k_x) \sin(k_y) - 2t'_2 \sin(2k_y) \quad (\text{S8})$$

$$g_{32} = \Delta + 2t'_1 \cos(k_x) + 2t_2 \cos(2k_x) - 2t'_2 \cos(2k_y) - 4t_2 \cos(k_x) \cos(k_y) \quad (\text{S9})$$

$$g_{33} = -2t_2 \sin(2k_x). \quad (\text{S10})$$

One can easily check that this Hamiltonian respects the reflection symmetry: $\hat{m}_x H(k_x, k_y) \hat{m}_x^{-1} = H(-k_x, k_y)$ with $\hat{m}_x = \tau_1 \otimes \sigma_3$, $\hat{m}_y H(k_x, k_y) \hat{m}_y^{-1} = H(k_x, -k_y)$ with $\hat{m}_y = \tau_1 \otimes \sigma_1$, and the particle-hole symmetry: $\Pi H(k_x, k_y) \Pi^{-1} = -H(-k_x, -k_y)$ with $\Pi = \tau_3 \otimes \sigma_0 \kappa$.

2. INEQUIVALENCE BETWEEN WANNIER AND EDGE ENERGY SPECTRA

It has been shown in Ref. [S1] that the edge energy spectrum can be smoothly deformed to the Wannier spectrum without closing the gap, implying that these two spectra are topologically connected. This statement is equivalent to saying that the Wannier bands at the Wannier chemical potential [S2] and the corresponding edge energy bands always close their gaps simultaneously. In the following, we will show that these two gaps do not necessarily vanish at the same time in our model Hamiltonian.

Let us consider a gapped Hamiltonian $H(\mathbf{k})$ in momentum space. We define the projection operator to the occupied bands as $\tilde{P}(\mathbf{k}) = \sum_{n=1}^{N_{\text{occ}}} |u_{\mathbf{k}}^n\rangle \langle u_{\mathbf{k}}^n|$ with $|u_{\mathbf{k}}^n\rangle$ being an occupied eigenstate of $H(\mathbf{k})$. The representation of this operator in the real space is obtained by Fourier transformation in the direction perpendicular to an edge,

$$P_{r\alpha,s\beta}(\mathbf{k}_{\parallel}) = \int_{BZ} \frac{dk_{\perp}}{2\pi} e^{ik_{\perp}(r-s)} \tilde{P}_{\alpha,\beta}(\mathbf{k}) \quad (\text{S11})$$

where r, s are coordinates of lattices in the edge-normal direction and α, β are orbital indices. \mathbf{k}_{\parallel} and k_{\perp} denote the momentum parallel and perpendicular to the edge, respectively.

Following Refs. [S1, S2], we construct a Hamiltonian from the projection operator,

$$H_e^0 = P V_0(x) P + (I - P), \quad (\text{S12})$$

where

$$V_0(x) = \begin{cases} 1 & \text{for } x < 0 \\ -1 & \text{for } x \geq 0 \end{cases} \quad (\text{S13})$$

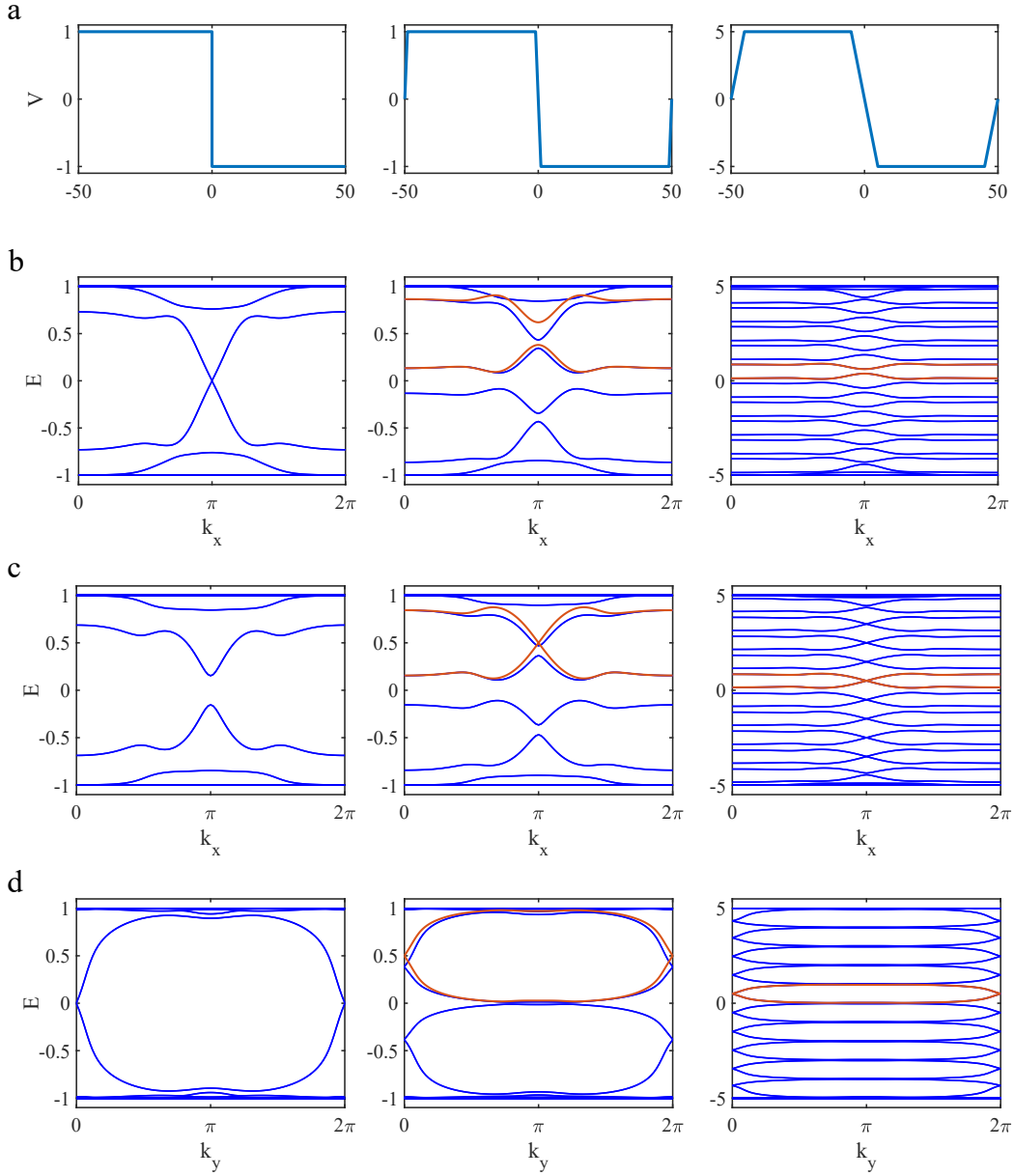


FIG. S1. (Color online) The connection between the edge energy spectrum and Wannier spectrum. a, Visualization of the edge potential for V_0 in the left column as well as V_L with $M = 1$ and $M = 5$ in the middle and right columns, respectively. b, The energy bands of H_e^0 (H_e^L) with $V_0(y)$ ($V_L(y)$) versus k_x in the left column (in the middle and right columns) for $\gamma = 0.34$. The edge energy spectrum encoded in H_e^0 has a vanishing gap, while the Wannier spectrum encoded in H_e^L for a moderate or large M (e.g., $M = 5$) has a finite gap. c, The same spectrum as b for $\gamma = 0.12$. The edge energy spectrum has a finite gap, which gradually vanishes as M is increased for $V_L(y)$, leading to a gapless Wannier spectrum. d, The energy spectrum of H_e^0 (H_e^L) with $V_0(x)$ ($V_L(x)$) versus k_y in the left column (in the middle and right columns). In this scenario, both the edge energy spectrum and Wannier spectrum are gapless. In the middle and right columns for b-d, the Wannier spectra are plotted as the red lines in comparison with the energy spectrum of H_e^L , showing that the former agrees very well with the latter for $M = 5$. For b-d, the middle and right columns correspond to the results for $M = 1$ and $M = 5$, respectively.

For a tight-binding model, x is the coordinate of discrete lattice sites along the direction perpendicular to the edge and takes the value of integer numbers from $-N_x/2$ to $(N_x/2 - 1)$ with N_x being the size along the x direction. Here, $V_0(x)$ introduces two boundaries at $x = 0$ and $x = N_x/2$ so that for $-N_x/2 \leq x < 0$, the system is topologically trivial and, otherwise, topologically equivalent to $H(\mathbf{k})$. Indeed, we have found that the eigenvalues $E_{V_0}(k_y)$ of $H_e^0(k_y)$ can be adiabatically mapped to the energy spectrum of the original Hamiltonian under open boundary conditions along x .

To see the connection between the edge energy spectrum and the Wannier band, we impose a linear edge so that the Hamiltonian reads

$$H_e^L = PV_L(x)P + M(I - P), \quad (\text{S14})$$

where the deformed linear edge potential is given by

$$V_L(x) = \begin{cases} x + N_x/2 & \text{for } -N_x/2 \leq x < -N_x/2 + M \\ M & \text{for } -N_x/2 + M \leq x < -M + 1 \\ -x & \text{for } -M + 1 \leq x < M \\ -M & \text{for } M \leq x < N_x/2 - M + 1 \\ x - N_x/2 & \text{for } N_x/2 - M + 1 \leq x < N_x/2 \end{cases} \quad (\text{S15})$$

Here, M is used to control the size of the linear potential region. When $M = 1$, $V_L(x)$ is only slightly deformed from $V_0(x)$. Ref. [S1] argues that this slight change should not significantly change the energy spectrum and thus as one continuously deform the boundary by increasing M for $V_L(x)$, the energy spectrum should be smoothly deformed into the eigenvalues of PxP , the restriction of which to the interval $[0, 1]$ gives exactly the Wannier spectrum. Therefore, they conclude that the edge energy spectrum and the Wannier spectrum should be topologically equivalent.

However, we find that this argument is not always true. For example, in our model, when $\gamma = 0.34$, the energy spectrum is gapless under the potential $V_0(y)$, which is consistent with our results under open boundary condition along y . But, as we slightly deform the boundaries, e.g., taking $M = 1$ for $V_L(y)$, we find that the energy gap opens, as shown in Fig. S1(b). When we further increase M to 5, the gap remains open and the energy spectrum is exactly the same as the Wannier spectrum.

We also show that for $\gamma = 0.12$, the energy gap vanishes for $M = 5$ while there is a nonzero energy gap for the energy spectrum under the boundary geometry $V_0(y)$ (see Fig. S1(c)). We indeed also find the case where the energy gap always remains gapless. For example, for $\gamma = 1.03$, the gap remains zero as we continuously deform the boundaries, as shown in Fig. S1(d).

Therefore, we conclude that the edge energy bands and Wannier bands are not guaranteed to close their gaps simultaneously and thus can be topologically inequivalent.

3. TOPOLOGICALLY TRIVIAL PHASE

In this section, we display richer physics in the topologically trivial phase as shown in Fig. S2. We find four regions corresponding to distinct $N_{\nu_\lambda}^0$ ($\lambda = x, y$): $(N_{\nu_x}^0, N_{\nu_y}^0) = (0, 0), (4, 0), (2, 0), (2, 2)$, even though they all have zero quadrupole moments and edge polarizations. This is reasonable as the edge states of the Wannier spectrum with zero Wannier centers do not contribute to the dipole moments. Despite being topologically trivial, these phases can have nonzero Wannier-sector polarization when odd number of pairs of edge states of the Wannier spectrum exists with zero eigenvalues. In particular, in the region with $(N_{\nu_x}^0, N_{\nu_y}^0) = (2, 2)$, although both Wannier-sector polarizations are nonzero, i.e., $(p_y^{\nu_x}, p_x^{\nu_y}) = (1/2, 1/2)$, the quadrupole moment and edge polarizations do not exist, implying the breakdown of the Wannier-sector polarizations to characterize the edge polarization and the quadrupole moments.

4. A TOPOLOGICAL INVARIANT FOR A WILSON LINE

A. Generic symmetry constraint of a Wilson line

Let us consider a generic symmorphic lattice symmetry: $\mathbf{r} \rightarrow D_g \mathbf{r}$, described by

$$gH(\mathbf{k})g^{-1} = H(D_g \mathbf{k}), \quad (\text{S16})$$

where g is a representation of the symmetric operation in momentum space, which is unitary. If $|u_{\mathbf{k}}^n\rangle$ is an eigenstate of $H(\mathbf{k})$ corresponding to the eigenenergy $E_{\mathbf{k}}^n$, then $g|u_{\mathbf{k}}^n\rangle$ is an eigenstate of $H(D_g \mathbf{k})$ corresponding to the same energy. As a result, we can write $g|u_{\mathbf{k}}^n\rangle$ in terms of eigenstates of $H(D_g \mathbf{k})$,

$$g|u_{\mathbf{k}}^n\rangle = \sum_{m=1}^{N_{\text{occ}}} |u_{D_g \mathbf{k}}^m\rangle \langle u_{D_g \mathbf{k}}^m | g | u_{\mathbf{k}}^n \rangle = \sum_{m=1}^{N_{\text{occ}}} |u_{D_g \mathbf{k}}^m\rangle B_{g, \mathbf{k}}^{mn}, \quad (\text{S17})$$

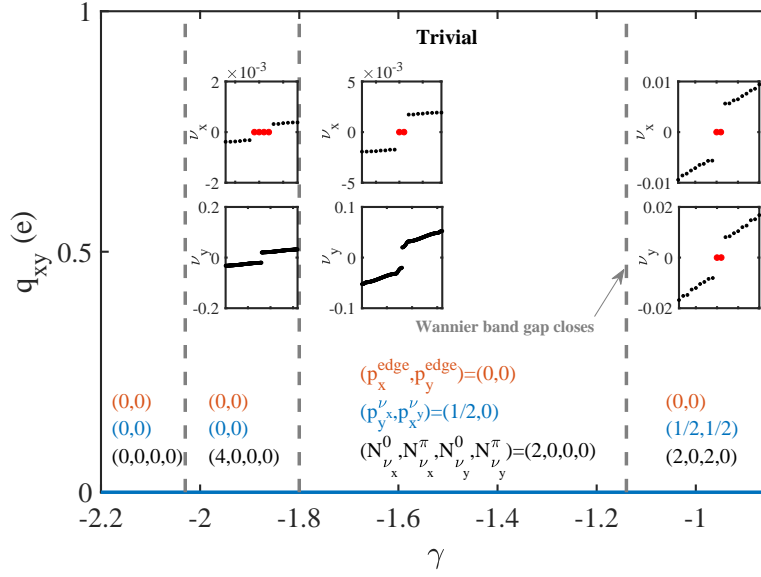


FIG. S2. (Color online) Distinct regions in topologically trivial insulators. The subsets display the Wannier spectrum ν_x (ν_y) for periodic boundary conditions along x (y) and open ones along y (x) with the isolated Wannier centers highlighted by red circles. The edge polarization $(p_x^{\text{edge}}, p_y^{\text{edge}})$, the Wannier-sector polarization $(p_y^{\nu_x}, p_x^{\nu_y})$, the number of edge states of the Wannier Hamiltonian $N_\nu \equiv (N_{\nu_x}^0, N_{\nu_x}^\pi, N_{\nu_y}^0, N_{\nu_y}^\pi)$ are also shown. The vertical dashed lines represent the critical points where the Wannier spectrum gap closes.

where $B_{g,\mathbf{k}}^{mn} = \langle u_{D_g\mathbf{k}}^m | g | u_{\mathbf{k}}^n \rangle$ is a unitary sewing matrix that connects states at \mathbf{k} with states at $D_g\mathbf{k}$. Since we are interested in the occupied bands, the superscript only enumerates the occupied states from 1 to the total number of the occupied states N_{occ} .

We now define the Wilson line following a path C in momentum space from \mathbf{k}_i to \mathbf{k}_f as

$$\mathcal{W}_{C, \mathbf{k}_f \leftarrow \mathbf{k}_i} = F_{\mathbf{k}_f - \Delta\mathbf{k}_{N-1}} \cdots F_{\mathbf{k}_i + \Delta\mathbf{k}_1} F_{\mathbf{k}_i}, \quad (\text{S18})$$

where $[F_{\mathbf{k}_{j'}}]^{mn} = \langle u_{\mathbf{k}_{j'} + \Delta\mathbf{k}_{j'+1}}^m | u_{\mathbf{k}_{j'}}^n \rangle$ with m and n being the indices for the occupied bands and $\Delta\mathbf{k}_j$ dividing the trajectory into N segments and $j' = 0, 1, \dots, N-1$ and $\mathbf{k}_{j'} = \mathbf{k}_i + \sum_{j=1}^{j'} \Delta\mathbf{k}_j$. In the limit $N \rightarrow \infty$, we can write the Wilson line in the following compact form,

$$\mathcal{W}_{C, \mathbf{k}_f \leftarrow \mathbf{k}_i} = \lim_{N \rightarrow \infty} \prod_{n=1}^{N-1} (I - i \Delta\mathbf{k}_n \cdot \mathcal{A}_{\mathbf{k}_n}) = \exp(-i \int_{\mathbf{k}_i}^{\mathbf{k}_f} \mathcal{A}_{\mathbf{k}} \cdot d\mathbf{k}), \quad (\text{S19})$$

where $[A_{\mathbf{k}}]^{mn} = -i \langle u_{\mathbf{k}}^m | \partial_{\mathbf{k}} u_{\mathbf{k}}^n \rangle$ is the non-Abelian Berry connection. Since $\int_{\mathbf{k}_i}^{\mathbf{k}_f} \mathcal{A}_{\mathbf{k}} \cdot d\mathbf{k}$ is a Hermitian matrix, the Wilson loop is unitary, reminiscent of a time evolution operator.

Since $|u_{\mathbf{k}}^n\rangle = g^\dagger \sum_m |u_{D_g\mathbf{k}}^m\rangle B_{g,\mathbf{k}}^{mn}$, we have

$$[F_{\mathbf{k}_j}]^{mn} = \sum_{m', n'} (B_{g, \mathbf{k}_{j+1}}^\dagger)^{mm'} \langle u_{D_g\mathbf{k}_{j+1}}^{m'} | u_{D_g\mathbf{k}_j}^{n'} \rangle B_{g, \mathbf{k}_j}^{n'n}, \quad (\text{S20})$$

leading to

$$\mathcal{W}_{C, \mathbf{k}_f \leftarrow \mathbf{k}_i} = B_{g, \mathbf{k}_f}^\dagger \mathcal{W}_{D_g C, D_g \mathbf{k}_f \leftarrow D_g \mathbf{k}_i} B_{g, \mathbf{k}_i}, \quad (\text{S21})$$

which can be equivalently expressed as

$$B_{g, \mathbf{k}_f} \mathcal{W}_{C, \mathbf{k}_f \leftarrow \mathbf{k}_i} B_{g, \mathbf{k}_i}^\dagger = \mathcal{W}_{D_g C, D_g \mathbf{k}_f \leftarrow D_g \mathbf{k}_i} = \mathcal{W}_{D_g \mathbf{k}_f \leftarrow D_g \mathbf{k}_i}, \quad (\text{S22})$$

where $D_g C$ denotes a new path obtained by applying the symmetry operation on the original path C (we will skip this notation for simplicity).

B. Reflection symmetry constraint and topological invariants

We now consider the reflection symmetry M_x , which, based on Eq. (S22), gives

$$B_{m_x, \mathbf{k}_f} \mathcal{W}_{x, \mathbf{k}} B_{m_x, \mathbf{k}_i}^\dagger = \mathcal{W}_{x, (-k_x - 2\pi, k_y) \leftarrow (-k_x, k_y)} = \mathcal{W}_{-x, M_x \mathbf{k}}, \quad (\text{S23})$$

where $\mathcal{W}_{x, \mathbf{k}}$ and $\mathcal{W}_{-x, \mathbf{k}}$ are defined as

$$\mathcal{W}_{x, \mathbf{k}} = \mathcal{W}_{(k_x + 2\pi, k_y) \leftarrow (k_x, k_y)}, \quad (\text{S24})$$

$$\mathcal{W}_{-x, \mathbf{k}} = \mathcal{W}_{(k_x - 2\pi, k_y) \leftarrow (k_x, k_y)}, \quad (\text{S25})$$

with x and $-x$ labelling the direction that a Wilson loop is obtained. Since the Wilson loop is unitary, we can write it as

$$\mathcal{W}_{x, \mathbf{k}}^{(0)} = \mathcal{W}_{x, (0, k_y)} = e^{iH_{\mathcal{W}_x}^{(0)}(k_y)}, \quad (\text{S26})$$

where $H_{\mathcal{W}_x}^{(0)}(k_y) = -i \log(\mathcal{W}_{x, \mathbf{k}}^{(0)})$ is the Wannier Hamiltonian for $k_x = 0$. Given that the Wannier Hamiltonian is a multivalued function of the Wilson loop, we redefine it with respect to a logarithm branch cut ϵ ,

$$H_{\mathcal{W}_x}^\epsilon(k_y) = -i \log_\epsilon(\mathcal{W}_{x, \mathbf{k}}^{(0)}), \quad (\text{S27})$$

where we take $\log_\epsilon e^{i\phi} = i\phi$, for $\epsilon \leq \phi < \epsilon + 2\pi$.

Now we can obtain the symmetry constraint on the Wannier Hamiltonian,

$$B_{m_x, (0, k_y)} H_{\mathcal{W}_x}^\epsilon(k_y) B_{m_x, (0, k_y)}^\dagger = -H_{\mathcal{W}_x}^{-\epsilon}(k_y) + 2\pi I_{N_{\text{occ}}} = -H_{\mathcal{W}_x}^{-\epsilon+2\pi}(k_y) + 4\pi I_{N_{\text{occ}}}. \quad (\text{S28})$$

Proof.

$$\begin{aligned} & B_{m_x, (0, k_y)} H_{\mathcal{W}_x}^\epsilon(k_y) B_{m_x, (0, k_y)}^\dagger \\ &= -i B_{m_x, (0, k_y)} \log_\epsilon(\mathcal{W}_{x, \mathbf{k}}^{(0)}) B_{m_x, (0, k_y)}^\dagger \\ &= -i \log_\epsilon \left[B_{m_x, (0, k_y)} \mathcal{W}_{x, \mathbf{k}}^{(0)} B_{m_x, (0, k_y)}^\dagger \right] \\ &= -i \log_\epsilon \left[\mathcal{W}_{-x, \mathbf{k}}^{(0)} \right] \\ &= -i \log_\epsilon \left[(\mathcal{W}_{x, \mathbf{k}}^{(0)})^{-1} \right] \\ &= -i \sum_n \log_\epsilon(e^{-i\nu_x^{(n)}}) |\nu_x^{(n)}\rangle \langle \nu_x^{(n)}| \\ &= -i \sum_n \left[-\log_{-\epsilon}(e^{i\nu_x^{(n)}}) + 2\pi i \right] |\nu_x^{(n)}\rangle \langle \nu_x^{(n)}| = -H_{\mathcal{W}_x}^{-\epsilon}(k_y) + 2\pi I_{N_{\text{occ}}} \end{aligned} \quad (\text{S29})$$

$$= -i \sum_n \left[-\log_{-\epsilon+2\pi}(e^{i\nu_x^{(n)}}) + 4\pi i \right] |\nu_x^{(n)}\rangle \langle \nu_x^{(n)}| = -H_{\mathcal{W}_x}^{-\epsilon+2\pi}(k_y) + 4\pi I_{N_{\text{occ}}}, \quad (\text{S30})$$

where $|\nu_x^{(n)}\rangle$ is the n th eigenvector of the Wilson loop $\mathcal{W}_{x, \mathbf{k}}^{(0)}$ corresponding to the eigenvalue $e^{i\nu_x^{(n)}}$. In the derivation, we have also used the following relations

$$\log_\epsilon(e^{-i\phi}) = -\log_{-\epsilon}(e^{i\phi}) + 2\pi i \quad (\text{S31})$$

$$\log_{-\epsilon}(e^{i\phi}) = \log_{-\epsilon+2\pi}(e^{i\phi}) - 2\pi i. \quad (\text{S32})$$

□

We now define the Wilson line with respect to ϵ by

$$\mathcal{W}_{k_x \leftarrow 0}^\epsilon(k_y) \equiv \mathcal{W}_{k_x \leftarrow 0}(k_y) \exp(-iH_{\mathcal{W}_x}^\epsilon(k_y) \frac{k_x}{2\pi}), \quad (\text{S33})$$

where $\mathcal{W}_{k_x \leftarrow 0}(k_y) \equiv \mathcal{W}_{(k_x, k_y) \leftarrow (0, k_y)}$. It can be easily checked that $\mathcal{W}_{2\pi \leftarrow 0}^\epsilon(k_y) = I_{N_{\text{occ}}}$, implying that $\mathcal{W}_{k_x \leftarrow 0}^\epsilon(k_y)$ is periodic with respect to k_x .

In the following, we will prove the symmetry constraints on the Wilson line with respect to ϵ ,

$$B_{m_x, (k_x, k_y)} \mathcal{W}_{k_x \leftarrow 0}^\epsilon(k_y) B_{m_x, (0, k_y)}^\dagger = \mathcal{W}_{-k_x+2\pi \leftarrow 0}^{-\epsilon}(k_y) \exp(-ik_x) = \mathcal{W}_{-k_x+2\pi \leftarrow 0}^{-\epsilon+2\pi}(k_y) \exp(-2ik_x). \quad (\text{S34})$$

Proof. We can directly obtain

$$B_{m_x, (k_x, k_y)} \mathcal{W}_{k_x \leftarrow 0}^\epsilon(k_y) B_{m_x, (0, k_y)}^\dagger = B_{m_x, (k_x, k_y)} \mathcal{W}_{k_x \leftarrow 0}(k_y) B_{m_x, (0, k_y)}^\dagger B_{m_x, (0, k_y)} e^{-iH_{W_x}^\epsilon(k_y) \frac{k_x}{2\pi}} B_{m_x, (0, k_y)}^\dagger \quad (\text{S35})$$

$$= \mathcal{W}_{-k_x \leftarrow 0}(k_y) e^{iH_{W_x}^\epsilon(k_y) \frac{k_x}{2\pi}} e^{-ik_x} = \mathcal{W}_{-k_x \leftarrow 0}^{-\epsilon} e^{-ik_x} \quad (\text{S36})$$

$$= \mathcal{W}_{-k_x \leftarrow 0}(k_y) e^{iH_{W_x}^{-\epsilon+2\pi}(k_y) \frac{k_x}{2\pi}} e^{-2ik_x} = \mathcal{W}_{-k_x \leftarrow 0}^{-\epsilon+2\pi} e^{-2ik_x}. \quad (\text{S37})$$

With the aid of the following equation

$$\mathcal{W}_{k_x+2\pi \leftarrow 0}^\epsilon(k_y) = \mathcal{W}_{k_x+2\pi \leftarrow 0}[\mathcal{W}_{2\pi \leftarrow 0}(k_y) \exp(-iH_{W_x}^\epsilon)] \exp(-iH_{W_x}^\epsilon \frac{k_x}{2\pi}) \quad (\text{S38})$$

$$= \mathcal{W}_{k_x \leftarrow 0}(k_y) \exp(-iH_{W_x}^\epsilon \frac{k_x}{2\pi}) \quad (\text{S39})$$

$$= \mathcal{W}_{k_x \leftarrow 0}^\epsilon(k_y), \quad (\text{S40})$$

we obtain Eq. (S34). \square

At $k_x = \pi$, $\epsilon = 0$ or $\epsilon = \pi$, Eq. (S34) leads to

$$B_{m_x, (\pi, k_y)} \mathcal{W}_{\pi \leftarrow 0}^{\epsilon=0}(k_y) B_{m_x, (0, k_y)}^\dagger = -\mathcal{W}_{\pi \leftarrow 0}^{\epsilon=0}(k_y) \quad (\text{S41})$$

$$B_{m_x, (\pi, k_y)} \mathcal{W}_{\pi \leftarrow 0}^{\epsilon=\pi}(k_y) B_{m_x, (0, k_y)}^\dagger = \mathcal{W}_{\pi \leftarrow 0}^{\epsilon=\pi}(k_y). \quad (\text{S42})$$

Let us present a theorem, showing that $B_{m_x, (\pi, k_y)} = B_{m_x, (0, k_y)}$ in a specific basis.

Theorem .1. Consider a Hamiltonian $H(\mathbf{k})$ describing an insulator at half filling. Suppose it respects reflection symmetry such that $\hat{m}_x H(\mathbf{k}) \hat{m}_x^\dagger = H(-k_x, k_y)$ and $\hat{m}_y H(\mathbf{k}) \hat{m}_y^\dagger = H(k_x, -k_y)$ with \hat{m}_x and \hat{m}_y anticommuting with each other. There exists a basis in which the sewing matrix takes the form

$$B_{m_x, (\pi, k_y)} = B_{m_x, (0, k_y)} = \begin{pmatrix} I_{N_{\text{occ}}/2} & 0 \\ 0 & -I_{N_{\text{occ}}/2} \end{pmatrix}. \quad (\text{S43})$$

Proof. From definition of the sewing matrix, we have

$$B_{m_x, (0, k_y)}^{mn} = \langle u_{(0, k_y)}^m | \hat{m}_x | u_{(0, k_y)}^n \rangle \quad (\text{S44})$$

$$B_{m_x, (\pi, k_y)}^{mn} = \langle u_{(\pi, k_y)}^m | \hat{m}_x | u_{(\pi, k_y)}^n \rangle. \quad (\text{S45})$$

Because $\hat{m}_x^2 = 1$, there are two eigenvalues: $\lambda = \pm 1$ for \hat{m}_x . If $|m_\lambda\rangle$ is an eigenvector of \hat{m}_x corresponding to an eigenvalue λ , then $\hat{m}_y |m_\lambda\rangle$ is another eigenvector of \hat{m}_x with an eigenvalue being $-\lambda$, since $\hat{m}_x \hat{m}_y |m_\lambda\rangle = -\hat{m}_y \hat{m}_x |m_\lambda\rangle = -\lambda \hat{m}_y |m_\lambda\rangle$ arising from the anticommutation relation of \hat{m}_x and \hat{m}_y , i.e., $\{\hat{m}_x, \hat{m}_y\} = 0$. In addition, if two eigenvectors $|m_\lambda^1\rangle$ and $|m_\lambda^2\rangle$ are orthogonal, i.e., $\langle m_\lambda^2 | m_\lambda^1 \rangle = 0$, then $\langle m_\lambda^2 | \hat{m}_y^\dagger \hat{m}_y | m_\lambda^1 \rangle = 0$. This tells us that the eigenvectors of \hat{m}_x come in pairs with eigenvalues ± 1 .

Let us choose a basis $\beta = \beta_1 \cup \beta_{-1}$ consisting of eigenvectors of \hat{m}_x , $\beta_1 = \{|m_1^1\rangle, \dots, |m_1^{N_{\text{occ}}}\rangle\}$ and $\beta_{-1} = \{\hat{m}_y |m_1^1\rangle, \dots, \hat{m}_y |m_1^{N_{\text{occ}}}\rangle\}$, where N_{occ} is the number of occupied states at half filling for a fixed momentum. Because of the reflection symmetry along x respected by the Hamiltonian, at $k_x = 0$ or π , the Hamiltonian commutes with \hat{m}_x , i.e., $[H(k_x = 0, k_y), \hat{m}_x] = 0$. As a result, in the basis β , $H(k_x = 0, k_y)$ takes the following block form,

$$H(k_x = 0, k_y) = \begin{pmatrix} H_1(k_y) & 0 \\ 0 & H_{-1}(k_y) \end{pmatrix}, \quad (\text{S46})$$

where H_λ with $\lambda = \pm 1$ are $N_{\text{occ}} \times N_{\text{occ}}$ matrices.

If $|u_1(k_y = 0)\rangle$ is an eigenstate of $H_1(k_y = 0)$ corresponding to an eigenenergy $E_1(k_y = 0)$, then $\hat{m}_y |u_1(k_y = 0)\rangle$ is an eigenstate of $H_{-1}(k_y = 0)$ with the same energy because $H \hat{m}_y |u_1(k_y = 0)\rangle = E_1(k_y = 0) \hat{m}_y |u_1(k_y = 0)\rangle$ and $\hat{m}_y |u_1(k_y = 0)\rangle \in \text{span}\{\beta_{-1}\}$. This tells us that, at half filling, only half of eigenstates of H_1 and H_{-1} are occupied. Consider an occupied basis $\beta_{\text{occ}} = \beta_{\text{occ}, 1} \cup \beta_{\text{occ}, -1}$ with $\beta_{\text{occ}, \lambda} = \{|u_{\lambda, (k_x=0, k_y=0)}^1\rangle, \dots, |u_{\lambda, (k_x=0, k_y=0)}^{N_{\text{occ}}/2}\rangle\}$ with $\lambda = \pm 1$, where $|u_{\lambda, (k_x=0, k_y=0)}^j\rangle$ with $j = 1, \dots, N_{\text{occ}}/2$ being eigenstates of $H_\lambda(k_x = 0, k_y = 0)$. In this basis,

$$B_{m_x, (0, 0)} = \begin{pmatrix} I_{N_{\text{occ}}/2} & 0 \\ 0 & -I_{N_{\text{occ}}/2} \end{pmatrix}, \quad (\text{S47})$$

where $I_{N_{\text{occ}}/2}$ is a $N_{\text{occ}}/2 \times N_{\text{occ}}/2$ identity matrix. For nonzero k_y , the number of occupied states in H_1 or H_{-1} should remain unchanged; otherwise, the Hamiltonian would not be an insulator. For example, if $|u_{\lambda, (k_x=0, k_y=0)}^1\rangle$ becomes unoccupied as we continuously vary k_y , its energy must intersect with the Fermi level, leading to a metallic phase instead of an insulating phase. This tells us that $B_{m_x, (k_x=0, \pi, k_y)}$ takes the same form as in Eq. (S47) in the basis $\beta_{\text{occ}, \lambda} = \{|u_{\lambda, (k_x=0, \pi, k_y)}^1\rangle, \dots, |u_{\lambda, (k_x=0, \pi, k_y)}^{N_{\text{occ}}/2}\rangle\}$ with $\lambda = \pm 1$, where $|u_{\lambda, (k_x=0, \pi, k_y)}^j\rangle$ with $j = 1, \dots, N_{\text{occ}}/2$ being eigenstates of $H_\lambda(k_x = 0, \pi, k_y)$, respectively. \square

Based on the above theorem, we can write Eq. (S41) and Eq. (S42) into

$$S\mathcal{W}_{\pi \leftarrow 0}^{\epsilon=0}(k_y)S^\dagger = -\mathcal{W}_{\pi \leftarrow 0}^{\epsilon=0}(k_y) \quad (\text{S48})$$

$$S\mathcal{W}_{\pi \leftarrow 0}^{\epsilon=\pi}(k_y)S^\dagger = \mathcal{W}_{\pi \leftarrow 0}^{\epsilon=\pi}(k_y), \quad (\text{S49})$$

where

$$S = \begin{pmatrix} I_{N_{\text{occ}}/2} & 0 \\ 0 & -I_{N_{\text{occ}}/2} \end{pmatrix}. \quad (\text{S50})$$

As a result,

$$\mathcal{W}_{\pi \leftarrow 0}^{\epsilon=0}(k_y) = \begin{pmatrix} 0 & U_+^{\epsilon=0}(k_y) \\ U_-^{\epsilon=0}(k_y) & 0 \end{pmatrix} \quad (\text{S51})$$

$$\mathcal{W}_{\pi \leftarrow 0}^{\epsilon=\pi}(k_y) = \begin{pmatrix} U_+^{\epsilon=\pi}(k_y) & 0 \\ 0 & U_-^{\epsilon=\pi}(k_y) \end{pmatrix}. \quad (\text{S52})$$

In our system, $N_{\text{occ}} = 2$ and thus $U_{\pm}^{\epsilon=0, \pi}(k_y)$ are complex numbers, we can define a winding number at $\epsilon = 0, \pi$ as

$$W_{\nu_x}^\epsilon = \frac{1}{2\pi i} \int_0^{2\pi} dk_y \partial_{k_y} \log(U_+^\epsilon(k_y)), \quad (\text{S53})$$

C. Gauge transformation

Since the Wilson line is determined by the occupied eigenstates of a Hamiltonian, the winding number of the Wilson line introduced in the preceding section may be dependent of the gauge transformation of the occupied eigenstates. Specifically, if we multiply a global phase to an occupied eigenstate, i.e., $|u_{k_x^*, k_y}^{m_x}\rangle \rightarrow e^{i\theta_{m_x}(k_x^*, k_y)}|u_{k_x^*, k_y}^{m_x}\rangle$ with $k_x^* = 0, \pi$ and a reflection eigenvalue $m_x = \pm 1$, then

$$\mathcal{W}_{\pi \leftarrow 0}^\epsilon(k_y) \rightarrow L^\dagger(k_x = \pi, k_y)\mathcal{W}_{\pi \leftarrow 0}^\epsilon(k_y)L(k_x = 0, k_y), \quad (\text{S54})$$

where

$$L(k_x, k_y) = \begin{pmatrix} e^{i\theta_{+1}(k_x, k_y)} & 0 \\ 0 & e^{i\theta_{-1}(k_x, k_y)} \end{pmatrix}. \quad (\text{S55})$$

This gives us the transformation for the Wilson line for $\epsilon = 0, \pi$,

$$\mathcal{W}_{\pi \leftarrow 0}^{\epsilon=0}(k_y) \rightarrow \begin{pmatrix} 0 & U_+^{\epsilon=0}(k_y)e^{i[\theta_{-1}(0, k_y) - \theta_{+1}(\pi, k_y)]} \\ U_-^{\epsilon=0}(k_y)e^{i[\theta_{+1}(0, k_y) - \theta_{-1}(\pi, k_y)]} & 0 \end{pmatrix} \quad (\text{S56})$$

$$\mathcal{W}_{\pi \leftarrow 0}^{\epsilon=\pi}(k_y) \rightarrow \begin{pmatrix} U_+^{\epsilon=\pi}(k_y)e^{i[\theta_{+1}(0, k_y) - \theta_{+1}(\pi, k_y)]} & 0 \\ 0 & U_-^{\epsilon=\pi}(k_y)e^{i[\theta_{-1}(0, k_y) - \theta_{-1}(\pi, k_y)]} \end{pmatrix}. \quad (\text{S57})$$

Thus, the winding number changes to

$$W_{\nu_x}^\epsilon \rightarrow \frac{1}{2\pi i} \int_0^{2\pi} dk_y \partial_{k_y} \log(U_+^\epsilon(k_y)e^{i\Theta^\epsilon(k_y)}) \quad (\text{S58})$$

$$= N_{\nu_x}^\epsilon + \frac{1}{2\pi} [\Theta^\epsilon(k_y = 2\pi) - \Theta^\epsilon(k_y = 0)], \quad (\text{S59})$$

where $\Theta^{\epsilon=0} \equiv \theta_{-1}(0, k_y) - \theta_{+1}(\pi, k_y)$, $\Theta^{\epsilon=\pi} \equiv \theta_{+1}(0, k_y) - \theta_{-1}(\pi, k_y)$. This shows that the global phase at $k_x = 0, \pi$ can produce an unphysical change of the winding number once the global phase exhibits a winding, implying that an

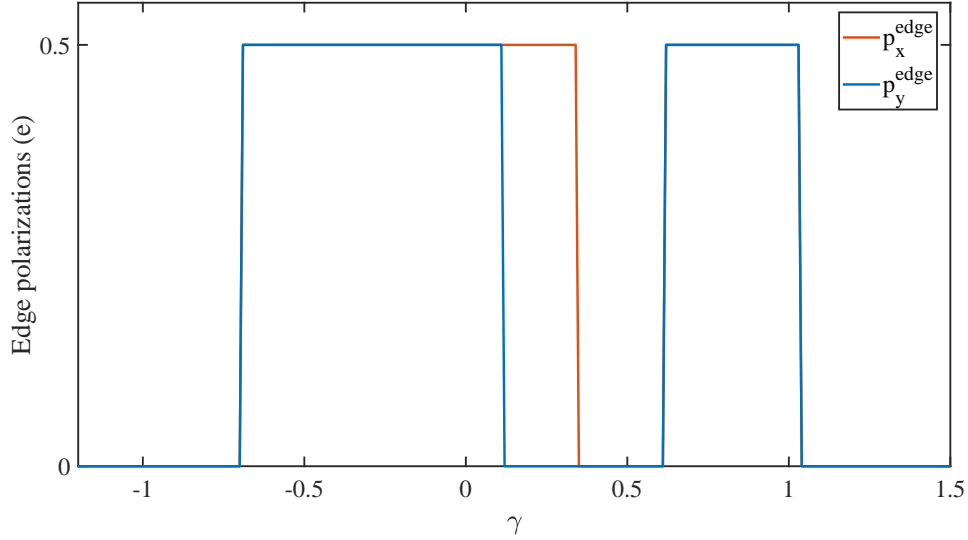


FIG. S3. (Color online) The edge polarizations calculated using the formula (6) in the main text. The edge polarization p_x^{edge} and p_y^{edge} in units of e are plotted as the red and blue lines, respectively.

isolated value of the winding number is not physical. However, if we maintain this global phase unchanged as we vary a system parameter and observe the change of the winding number, this change is physical and tells us that the edge polarization appears or disappears. This works as the polarization is a Z_2 quantity.

Numerically, we need to maintain the continuity of the global phase of the occupied energy states with respect to k_y along the reflection symmetric lines $k_x = 0$ and $k_x = \pi$ for a fixed system parameter γ and to maintain the continuity of the Berry phase of these states about k_y with respect to γ .

To maintain the continuity of the global phase with respect to k_y , we first make the wave function $|u_{k_x^*, k_y}^{m_x}\rangle$ continuous between two neighboring points (k_x^*, k_y) and $(k_x^*, k_y + \Delta k_y)$, where $k_y = n\Delta k_y$ with $\Delta k_y = \frac{2\pi}{N_y}$ and $n = 0, 1, \dots, (N_y - 1)$. To achieve this, we choose the maximum component of $\langle u_{k_x^*, k_y + \Delta k_y}^{m_x} | u_{k_x^*, k_y}^{m_x} \rangle$, that is,

$$n_{max} = \text{argmax}_n |([u_{k_x^*, k_y + \Delta k_y}^{m_x}]^n)^* [u_{k_x^*, k_y}^{m_x}]^n|, \quad (\text{S60})$$

and eliminate the numerical phase difference by the transformation,

$$|u_{k_x^*, k_y + \Delta k_y}^{m_x}\rangle \rightarrow \exp(-i\phi_1) |u_{k_x^*, k_y + \Delta k_y}^{m_x}\rangle, \quad (\text{S61})$$

where $\phi_1 = \text{Im} \log([u_{k_x^*, k_y + \Delta k_y}^{m_x}]^{n_{max}} / [u_{k_x^*, k_y}^{m_x}]^{n_{max}})$. We repeat this process from $k_y = 0$ to $k_y = 2\pi - \Delta k_y$. After that, we make the wave functions continuous between $k_y = 2\pi - \Delta k_y$ and $k_y = 0$ by performing the following phase transformations

$$|u_{k_x^*, n\Delta k_y}^{m_x}\rangle \rightarrow \exp(-i\phi_2(1 - n/N_y)) |u_{k_x^*, n\Delta k_y}^{m_x}\rangle, \quad (\text{S62})$$

where $\phi_2 = \text{Im} \log([u_{k_x^*, 0}^{m_x}]^{n_{max}} / [u_{k_x^*, 2\pi - \Delta k_y}^{m_x}]^{n_{max}})$ with $n_{max} = \text{argmax}_n |([u_{k_x^*, 0}^{m_x}]^n)^* [u_{k_x^*, 2\pi - \Delta k_y}^{m_x}]^n|$.

To make sure that the Berry phase of each occupied band about k_y along the reflection symmetric lines $k_x^* = 0, \pi$ is continuous as γ varies, we numerically compute the Berry phase based on the following formula

$$\nu_y^{\pm 1}(k_x^* = 0, \pi) = \text{Im} \lim_{N_y \rightarrow \infty} \sum_{n=0}^{N_y-1} \log \langle u_{k_x^*, (n+1)\Delta k_y}^{\pm 1} | u_{k_x^*, n\Delta k_y}^{\pm 1} \rangle \quad (\text{S63})$$

and perform a suitable transformation $|u_{k_x^*, k_y = n\Delta k_y}^{m_x}\rangle \rightarrow \exp(-i2\pi p \frac{n}{N_y}) |u_{k_x^*, k_y = n\Delta k_y}^{m_x}\rangle$ with p being an integer provided that the Berry phases between two neighboring γ change by $-2p\pi$. The procedure is similar for calculation of the winding number $W_{\nu_y}^\epsilon$.

In Fig. S3, we plot the edge polarizations $p_{x,y}^{\text{edge}}$ as a function of γ , which is calculated based on the formula (6) in the main text. The results are consistent with the Wannier spectrum in a cylinder geometry and the edge polarization calculated using the hybrid Wannier functions.

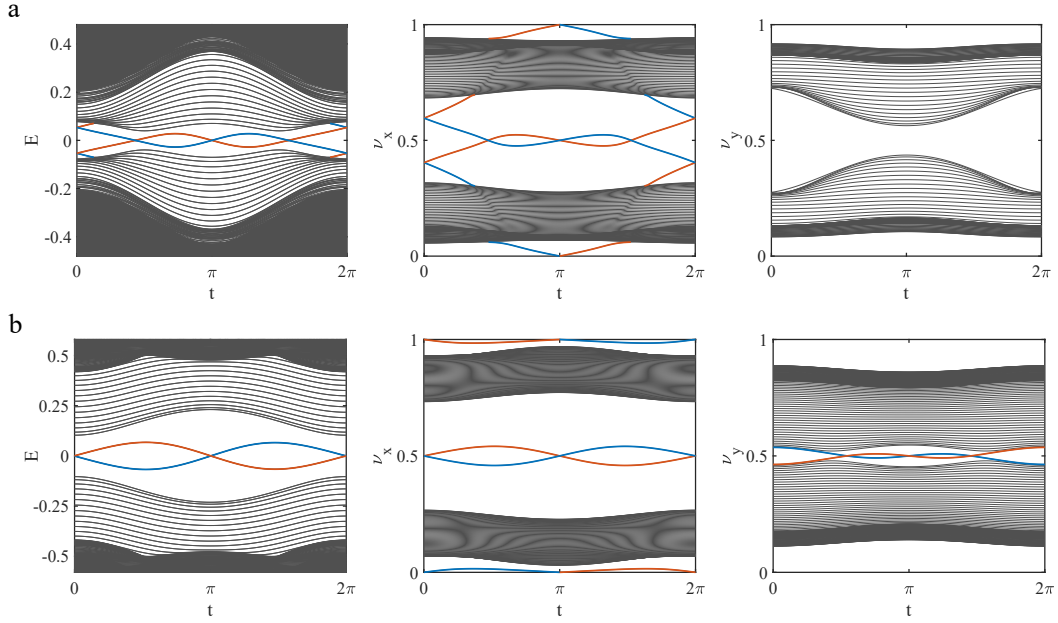


FIG. S4. (Color online) The energy spectrum and Wannier spectrum during the pumping process. a, The cycle from a topologically trivial phase to a type-II QTI and back to the trivial phase. b, The cycle from a type-II QTI to a type-I AQTI and back to the type-II QTI. For both a and b, the first column corresponds to the energy spectrum with open boundary along x and y and the second (third) column correspond to the Wannier spectrum ν_x (ν_y) with open boundary along y (x) and periodic boundary along x (y).

5. ENERGY AND WANNIER SPECTRA DURING A PUMPING PROCESS

In the main text, we have shown the transport of the corner charge, the quadrupole moment and the edge polarizations as system parameters vary over an entire cycle. In this section, we present the energy spectrum in an open boundary geometry (see the first column in Fig. S4) and the Wannier spectrum in a cylinder geometry (see the last two columns in Fig. S4) during this full process. The first row in the figure corresponds to the pump from a topologically trivial phase to a type-II QTI and then back to the trivial phase, while the second row to the pump from a type-II QTI to a type-I AQTI and then back to the original type-II phase. It is clear that we can divide the energy spectrum and Wannier spectrum into two bands with gaps between them. In the former scenario, we see that the corner states connect the lower energy band to the higher one as time evolves, which shows the chiral property of the corner states if time is regarded as a third momentum; this agrees well with the quantized transport of corner charges shown in the main text. For the Wannier spectrum ν_x , the edge states exist inside both the gaps around 0 and 1/2 and these states connect two bands of the Wannier spectrum as time progresses, similar to the energy spectrum. However, for the Wannier spectrum ν_y , we do not see the presence of the edge states connecting two Wannier bands, consistent with the zero net transport for the edge polarization p_y^{edge} . In the second pumping scenario, while the corner states exist during the full cycle, they do not connect the two energy bands, and thus are not "chiral", which is consistent with the zero transport of the corner charges. Similar band patterns occur in the Wannier spectrum ν_x . However, for the Wannier spectrum ν_y , we find the "chiral"-like edge states, which explains the presence of the net transport of the edge polarization p_y^{edge} shown in the main text.

6. EXPERIMENTAL REALIZATION

In this section, we discuss how to realize our Hamiltonian in electric circuits, in which the SSH model [S3], Weyl semimetal [S4] and type-I quadrupole topological insulator [S5] have been experimentally achieved. Let us consider an electrical network consisting of many nodes simulating sites in a tight-binding model. For each node m in the circuit, suppose that I_m is the external current flowing into this node and V_m is the voltage at this node with respect

to the ground, according to Kirchhoff's law, we have

$$I_m = \sum_n I_{mn} + I_{m0} = \sum_n X_{mn}(V_m - V_n) + X_m V_m, \quad (\text{S64})$$

where I_{mn} and I_{m0} are the current flowing from node m to n and from node m to the ground, respectively. $X_{mn} = 1/Z_{mn}$ is the admittance between node m and n with Z_{mn} the corresponding impedance, and $X_m = 1/Z_m$ is the admittance between node m and the ground. Writing I_m and V_m in the form of column vectors, we have

$$\mathbf{I} = J(\omega)\mathbf{V}, \quad (\text{S65})$$

where $J(\omega)$ denotes the circuit Laplacian with ω being the AC frequency of the input current.

By connecting appropriate capacitors, inductors and negative impedance converters with current inversion (INIC) [S6, S7] as shown in Fig. (4) in the main text, we can achieve a Laplacian simulating our Hamiltonian, i.e., $J = iH$. The sign of the resistance of a INIC depends on how it is connected. For example, for the configuration shown in Fig. (4) in the main text, the current from node 1 to node 2 within a unit cell is determined by $I_{12} = (V_1 - V_2)/(-R)$ corresponding to a negative resistance while the current from node 2 to node 1 determined by $I_{21} = (V_2 - V_1)/R$ corresponding to a positive resistance. To eliminate unnecessary onsite terms, we also need to add onsite impedances Z'_m as shown in Fig. 4. For the system with periodic boundary conditions, the values of $Z'_{a=1,2,3,4}$ are as follows,

$$\frac{1}{Z'_1} = \frac{1}{Z'_4} = (2t'_1 - 2t_2 - 2t'_2 + \Delta) + i(4t_1 + 2t'_1 + 6t_2 - 2t'_2) \quad (\text{S66})$$

$$\frac{1}{Z'_2} = \frac{1}{Z'_3} = (-2t'_1 + 2t_2 + 2t'_2 - \Delta) + i(2t'_1 + 2t_2 - 6t'_2 + 2\gamma). \quad (\text{S67})$$

We follow the experimental approach to directly measure the Green's function [S8]. Specifically, we apply an input current I_n at one node n of the circuit and measure the voltage $V_m^{(n)}$ at node m , giving us the single-point impedance,

$$G_{mn} = V_m^{(n)}/I_n, \quad (\text{S68})$$

which is a Green's function of the system Hamiltonian, i.e.,

$$G_{mn} = (J^{-1})_{mn}. \quad (\text{S69})$$

All the information, such as the energy spectrum and eigenstates, can be extracted from the Green's function.

To achieve our model, we consider an electric circuit composed of $N_x N_y$ unit cells; each unit cell contains 4 nodes and each node is labeled by (\mathbf{R}, α) . If we consider a torus geometry with periodic boundaries along both x and y , we only need to apply a current in one node $(\mathbf{0}, \beta)$ and measure the impedance $G_{\alpha\beta}(\mathbf{R})$ between the node (\mathbf{R}, α) and node $(\mathbf{0}, \beta)$ for all the different nodes (\mathbf{R}, α) , leading to the Green's function in momentum space,

$$G_{\alpha\beta}(\mathbf{k}) = \sum_{\mathbf{R}} G_{\alpha\beta}(\mathbf{R}) \exp(-i\mathbf{k} \cdot \mathbf{R}), \quad (\text{S70})$$

where \mathbf{k} is the momentum and $\sum_{\mathbf{R}}$ is the sum over all unit cells. Similarly, in a cylinder geometry, e.g., with open boundaries along y and periodic boundaries along x , only the impedance $Z_{\alpha\beta}((R_x, R_y), (0, R'_y)) = G_{\alpha\beta}((R_x, R_y), (0, R'_y))$ between the node $((R_x, R_y), \alpha)$ and node $((0, R'_y), \beta)$ is required to be probed, yielding the Green's function

$$G_{(R_y, \alpha)(R'_y, \beta)}(\mathbf{k}) = \sum_{R_x} G_{\alpha\beta}((R_x, R_y), (0, R'_y)) \exp(-ik_x R_x). \quad (\text{S71})$$

Once the Green's functions in the torus and cylinder geometry are measured, the quadrupole moment and edge polarizations can be obtained.

For the system with open boundary conditions, the presence of zero-energy corner states of the Hamiltonian will give rise to the divergence of the two-point impedance near the corners. Thus we can measure the corner modes through the measurement of the resonance of the impedance between two neighbouring nodes near the corners at the resonance frequency [S5].

* yongxuphy@tsinghua.edu.cn

- [S1] Fidkowski, L., Jackson, T. S. & Klich, I. Model characterization of gapless edge modes of topological insulators using intermediate Brillouin-zone functions. *Phys. Rev. Lett.* **107**, 036601 (2011).
- [S2] Khalaf, E., Benalcazar, W. A., Hughes, T. L., & Queiroz, R. Boundary-obstructed topological phases. Preprint at <https://arXiv.org/abs/1908.00011> (2019).
- [S3] Lee, C. H. et al. Topoelectrical Circuits. *Commun. Phys.* **1**, 39 (2018).
- [S4] Lu, Y. et al. Probing the Berry curvature and Fermi arcs of a Weyl circuit. *Phys. Rev. B* **99**, 020302(R) (2019).
- [S5] Imhof, S. et al. Topoelectrical-circuit realization of topological corner modes. *Nat. Phys.* **14**, 925-929 (2018).
- [S6] Chen, W. K. *The Circuits and Filters Handbook*, 3rd ed. (CRC Press, Inc., Boca Raton, FL, USA, 2009).
- [S7] Hofmann, T., Helbig, T., Lee, C. H., & Thomale, R. Chiral Voltage Propagation and Calibration in a Topoelectrical Chern Circuit. *Phys. Rev. Lett.* **122**, 247702 (2019).
- [S8] Helbig, T. et al. Band structure engineering and reconstruction in electric circuit networks. *Phys. Rev. B* **99**, 161114(R) (2019).